

JGR Solid Earth

RESEARCH ARTICLE

10.1029/2023JB027297

Key Points:

- A 25 mm-long bump of high normal stress can cause persistently complex rupture sequences on a 760 mm-long sample
- A sufficiently prominent bump ($\Delta\sigma_{bt}/\bar{\sigma}_n > 6$) can stop rupture; but slip can sometimes re-initiate on the other side of the bump
- A prominent bump can act as an asperity or a barrier depending on strength excess, resulting in a variety of event sizes

Correspondence to:

S. B. L. Cebry,
sarahbleach@gmail.com

Citation:

Cebry, S. B. L., Sorhaindo, K., & McLaskey, G. C. (2023). Laboratory earthquake rupture interactions with a high normal stress bump. *Journal of Geophysical Research: Solid Earth*, 128, e2023JB027297. <https://doi.org/10.1029/2023JB027297>

Received 21 JUN 2023

Accepted 30 OCT 2023

Author Contributions:

Conceptualization: Gregory C. McLaskey

Data curation: Sara B. L. Cebry, Kian Sorhaindo

Formal analysis: Sara B. L. Cebry, Kian Sorhaindo

Funding acquisition: Gregory C. McLaskey

Investigation: Sara B. L. Cebry, Kian Sorhaindo

Methodology: Sara B. L. Cebry, Kian Sorhaindo, Gregory C. McLaskey

Software: Sara B. L. Cebry, Gregory C. McLaskey

Supervision: Gregory C. McLaskey


Validation: Sara B. L. Cebry

Visualization: Sara B. L. Cebry, Kian Sorhaindo

Writing – original draft: Sara B. L. Cebry, Kian Sorhaindo

Writing – review & editing: Sara B. L. Cebry, Gregory C. McLaskey

Laboratory Earthquake Rupture Interactions With a High Normal Stress Bump

Sara B. L. Cebry¹ , Kian Sorhaindo¹ , and Gregory C. McLaskey¹ 

¹Cornell University, Ithaca, NY, USA

Abstract To better understand how normal stress heterogeneity affects earthquake rupture, we conducted laboratory experiments on a 760 mm poly (methyl-methacrylate) PMMA sample with a 25 mm “bump” of locally higher normal stress ($\Delta\sigma_{bt}$). We systematically varied the sample-average normal stress ($\bar{\sigma}_n$) and bump prominence ($\Delta\sigma_{bt}/\bar{\sigma}_n$). For bumps with lower prominence ($\Delta\sigma_{bt}/\bar{\sigma}_n < 6$) the rupture simply propagated through the bump and produced regular sequences of periodic stick-slip events. Bumps with higher prominence ($\Delta\sigma_{bt}/\bar{\sigma}_n > 6$) produced complex rupture sequences with variable timing and rupture sizes, and this complexity persisted for multiple stick-slip supercycles. During some events, the bump remained locked and acted as a barrier that completely stopped rupture. In other events, a dynamic rupture front terminated at the locked bump, but rupture reinitiated on the other side of the bump after a brief pause of 0.3–1 ms. Only when stress on the bump was near critical did the bump slip and unload built up strain energy in one large event. Thus, a sufficiently prominent bump acted as a barrier (energy sink) when it was far from critically stressed and as an asperity (energy source) when it was near critically stressed. Similar to an earthquake gate, the bump never acted as a permanent barrier. In the experiments, we resolve the above rupture interactions with a bump as separate rupture phases; however, when observed through the lens of seismology, it may appear as one continuous rupture that speeds up and slows down. The complicated rupture-bump interactions also produced enhanced high frequency seismic waves recorded with piezoelectric sensors.

Plain Language Summary Natural faults have complex geometries, but are idealized as planar surfaces in most models and laboratory setups. To study the effect of one isolated “bump” of high normal stress, we conducted laboratory experiments on a 760 mm poly (methyl-methacrylate) sample with a 25 mm long section of locally high normal stress. We varied both the average normal stress applied to the sample and the prominence of the bump to explore how more dramatic bumps could affect sequences of slip events. When the bump was small and stress was nearly uniform, the bump had little effect and the entire fault consistently slipped the same amount, at the same time. When the bump was large and the bump stress was much higher than stress elsewhere on the sample, different sections of the fault slipped independently resulting in complex sequences with large variations in event sizes. Smaller events slipped areas around the bump without slipping the bump. In some cases, the bump could be by-passed and the entire fault slipped, except the bump. But the bump was never able to permanently stop these slip events. Eventually, the bump was stressed close to its limit and slipped which created larger events than otherwise expected.

1. Introduction

Earthquakes are produced by dynamic rupture of faults within the Earth's crust. While faults are often idealized as planar interfaces, in reality they can contain bends, bumps, jogs, and stepovers that affect the distribution of stresses along the fault and may be important for the generation of foreshocks, aftershocks, and heterogeneous coseismic slip distributions. The multi-scale topography of faults (roughness), measured in laboratory and field studies (Brodsky et al., 2020; Candela & Brodsky, 2016; Power et al., 1987; Yamashita et al., 2021) likely produces regions of locally high normal stress (bumps) when compressed together. Fault stepovers or bends can also produce a similar localized increase in fault normal stress. Bumps with higher normal stress have higher strength and fracture energy and can act as “barriers” that cause rupture to arrest. These fault irregularities may stop an earthquake rupture, limit its size, and/or create characteristic earthquakes whose size and location are determined by specific fault features. However, it is also possible that a high strength bump can accumulate shear stress and finally slip a large amount, and therefore act as a seismic asperity (Aki, 1984). Thus, a bump may act as a barrier or an asperity under different circumstances.

Modeling studies dating back several decades have explored the effects of heterogeneous fault conditions. Das and Aki (1977) considered a 1D rupture that encountered barriers and found that the rupture can pass by and leave the barriers unbroken, but in some cases delayed rupture of the barriers can also occur. Dunham et al. (2003) studied a single barrier on a 2D fault plane and found that it initially delayed rupture, but once stress on the bump reached a critical level, the bump ruptured and released a slip velocity pulse that increased the rupture velocity. Other studies have specifically looked at heterogeneities due to normal stress. Schaal and Lapusta (2019) performed multi-cycle simulations with multiple normal stress bumps and found two scales of seismicity: small seismicity when only one bump ruptured and large seismic events where multiple bumps ruptured. Sudhir (2022) extended this to consider the strength of the heterogeneity and found that faults where the maximum stress on the bump was six times the average stress on the fault produced large-scale events that were preceded by multiple small-scale events. Zielke et al. (2017) modeled ruptures under varying roughness and observed less moment release on rougher faults.

On natural faults, geometric and stress heterogeneity are thought to cause spatially variable slip and rupture velocity. Lay and Kanamori (1981) and Lay et al. (1982) categorized faults based on an asperity model to explain the different behavior of historic earthquakes. Lay et al. (2012) extended this to subduction zones and proposed that different depth domains produce different seismic behavior due to variations in frictional, rheological, stress, and fluid properties. Another example of natural fault heterogeneity are earthquake gates which Oskin et al. (2015) defined as areas of fault complexity that conditionally stop ruptures (e.g., Aksay restraining double bend (Duan et al., 2019) and San Andreas fault and San Jacinto fault stepover (Rodriguez Padilla et al., 2022)). These gates control the probability of large, multi-fault ruptures which make earthquake hazard estimation difficult.

Several previous laboratory experiments explored fault heterogeneity by comparing smooth, saw-cut faults to faults that are rougher either due to preparation with differing abrasives (Ohnaka & Shen, 1999), natural wear (Xu et al., 2023), a fracturing process (Badt et al., 2016; Goebel et al., 2012), or a combination (Morad et al., 2022). These studies found that rough faults produce more variable slip behavior and were typically stronger and more dynamic than smoother faults. However, with this experimental approach, it is difficult to attribute observed changes in sample behavior to specific physical mechanisms.

Experimental studies of heterogeneities can be categorized as transient, which get erased with consecutive stick-slip events, or persistent, which remain regardless of fault slip. For example, transient stress heterogeneities due to loading irregularities typically produce confined events that become progressively larger with each event in the sequence (Ben-David et al., 2010; Ke et al., 2018; McLaskey, 2019; Wu & McLaskey, 2019). Similar studies measured the stress changes due to confined events and found that ruptures terminate by propagating into low stress regions (Bayart et al., 2018; Cebry, Ke, & McLaskey, 2022; Kammer et al., 2015; Ke et al., 2021). Elastic shear stress redistribution from the terminated rupture, increased shear stress in neighboring locked fault sections, and this prepared the fault for the next rupture to propagate further. The redistribution of shear stress caused the transient heterogeneities to be erased with consecutive slip events rather than persist in the same location throughout entire sequences.

Other experimental studies looked at normal stress heterogeneities that persist regardless of fault slip. One example is a nonuniform normal stress distribution that naturally occurs along a long laboratory sample, often with higher normal stress at the sample ends than in the center. In the case of Cebry, Ke, Shreedharan, et al. (2022), the ends of the sample acted as seismic asperities yet the stress levels between two asperities played an important role in determining whether rupture on one asperity triggered rupture on the other. Cebry, Ke, and McLaskey (2022) showed that direct fluid injection onto the fault could also promote contained rupture events. Steinhardt et al. (2023) investigated the effect of a normal stress asperity on the scale independence of stress drop. Buijze et al. (2020, 2021) observed normal stress heterogeneities from differential gouge compaction and highlighted nucleation complexity caused by normal stress variations and the importance of fault stress state.

While most of the above studies explored heterogeneity that occurred naturally as a result of sample boundaries, loading, or fluid injection, some experimental studies specifically imposed fault irregularities. McLaskey and Lockner (2018) studied a “pin” of intact rock transecting a saw-cut granite fault. Gounon et al. (2022) explored rupture nucleation on a polycarbonate sample with alternating rough and smooth fault sections. Other studies imposed a fracture energy barrier using a rock gouge layer (Rubino et al., 2022), a lubricant (Bayart et al., 2018), or other surface treatment (Gvirtzman & Fineberg, 2021).

The experiments in this study use two unique, composite poly (methyl-methacrylate) (PMMA) blocks that allow us to create a prominent bump on the fault while still having the blocks slide past one another similar to a set of

homogeneous blocks. In this work, we created a single “bump” of high normal stress (σ_b) at a known location near the center of the nominally planar laboratory fault. We believe that this bump, which spans the entire fault depth, behaves similar to an earthquake gate such as a double bend or restraining stepover (e.g., McClay & Bonora, 2001) which are both 1D features on a 2D fault plane; however, the bump in our study likely has relevance to other forms of fault roughness. In this work, we observed how dynamic ruptures interact with this bump over multiple stick-slip cycles. Furthermore, we systematically changed the sample-average normal stress ($\bar{\sigma}_n$) and the amplitude of bump ($\Delta\sigma_{bt}$), to see how those factors affect rupture initiation, propagation, and termination. We found that as the prominence of the bump ($\Delta\sigma_{bt}/\bar{\sigma}_n$) increased, the sample behavior switched from a set of identical, periodic stick-slip events that always rupture the entire fault surface to varying sequences that include partial and sample-spanning ruptures.

The complexity in slip behavior that resulted from bumps with large prominence arose when multiple smaller ruptures were required to increase stress on the bump to a critical level. In this case, the bump was significantly stronger than the rest of the fault, so at first, it acted as a barrier. However, partial rupture events on the rest of the fault systematically increased the shear stress levels on the bump. Once the bump was critically stressed and began to slip, it released a large amount of stress, proportional to its strength, and acted as an asperity. We also found that in some cases a rupture could be stopped by the bump then reinitiate on the other side of the bump, despite a lack of connection with the previously ruptured section.

2. Method

2.1. Definition of Variables

Throughout the paper we use several variables as defined in Table 1.

Table 1
Variables and Definitions Used Throughout the Paper

Variable	Definition
a	Shear crack half length
E	Elastic modulus, $E_{\text{PMMA}} = 2.6$ GPa (Kammer et al., 2012)
G	Shear modulus, $G_{\text{PMMA}} = 1.0$ GPa (Kammer et al., 2012)
L	Combined length of the moving and stationary block in the y -direction
t	Thickness of an individual shim
$\Delta\bar{x}$	Average apparent slip recorded on all eight displacement sensors in a 0.2 s window centered on the event
$\widehat{\Delta x}$	Variance of apparent slip near the bump normalized by the average apparent slip at that location over the entire experiment, calculated by $\text{var}\left(\frac{\Delta x_{Aj}}{\sum_{n=1}^k \frac{\Delta x_{An}}{k}}\right)$
$\Delta\sigma_{bt}$	Theoretical increase in stress above sample-average normal stress $\bar{\sigma}_n$ due to shims
$\Delta\tau(r)$	Shear stress increase at a distance r ahead of a Mode II crack tip
$\Delta\bar{\tau}_{\text{mech}}$	Change in sample-average shear stress due to a stick-slip events
ν	Poisson's ratio, $\nu_{\text{PMMA}} = 0.37$
σ_b	Absolute normal stress on the bump
$\bar{\sigma}_n$	Sample-average normal stress
$\sigma_n(x)$	Local normal stress
$\bar{\tau}$	Sample-average shear stress
$\tau(x)$	Local shear stress
$\tau_o - \tau_r$	Shear stress drop within a crack, initial minus residual shear stress
$\tau_o(x)$	Local initial shear stress prior to a stick-slip event
$\bar{\tau}_p$	Peak $\bar{\tau}$ measured as the maximum $\bar{\tau}$ prior to the initiation of slip
$\tau_p(x)$	Local peak $\tau(x)$ prior to a stick-slip event
μ_s	Static friction coefficient, assumed to be constant in space and time

2.2. Testing Procedure

In these experiments, a moving block and a stationary block were squeezed together in a biaxial load frame (Figure 1). An array of four hydraulic cylinders (C1-C4) applied a constant $\bar{\sigma}_n$ in the y -direction, perpendicular to the simulated fault, which is the interface between the stationary and moving block. Once set to the prescribed level, $\bar{\sigma}_n$ was held roughly constant by simply closing a valve to the hydraulic fluid. Another cylinder (C5) applied force in the x -direction to the moving block which increased the $\bar{\tau}$ on the fault plane. An electric pump was used to increase $\bar{\tau}$ at a constant rate and produce a long-term average slip rate of 0.2 $\mu\text{m/s}$. The moving block and cylinders (C1-C4) translated in the positive x -direction due to slip along both the simulated fault and along a low friction interface of Teflon against precision ground steel (Figure 1a).

Unlike previous experiments on this same loading apparatus (Cebry & McLaskey, 2021; McLaskey & Yamashita, 2017), both the moving block and stationary block were composed of many smaller PMMA “sub-blocks” that were squeezed together by hand-tensioned threaded rods running through pre-drilled holes that spanned the entire length of the sample in the x direction (Figure 1b, See Appendix A for details). The sub-blocks were not glued together, as shown in Figure 2, and could slip in the y -direction to accommodate large changes in $\sigma_n(x)$ while the tensioned rods held each composite block together so that it behaved similar to an intact, homogeneous block. The fault was prepared by sanding the PMMA surfaces with 80 grit sandpaper, however the fault surface was not perfectly planar due to variation in alignment of the sub-blocks. The sub-blocks were numbered, starting from the North end for both the moving block (MB#1–MB#30) and stationary block (SB#1–SB#33). PMMA was chosen for its compliance (shear modulus $G_{\text{PMMA}} \approx 1$ GPa), small nucleation length (approximately 10–100 mm (Cebry & McLaskey, 2021; Guérin-Marthe et al., 2019; McLaskey, 2019; Nielsen et al., 2010)), as well as machinability.

Thin steel shims were placed between a single sub-block in the PMMA sample and the steel load frame to create a bump of locally high normal stress, as shown in Figure 1c. The steel shims measured 25 mm by 0.838 mm by 38 mm (x, y, z directions) and were placed at MB#13 ($x = 305$ mm) and SB#14 ($x = 317$ mm) (Figure 1). For tests with two shims, both shims were placed only on MB#13. For the tests with four and six shims, half of the shims were placed on SB#14 and the other half on MB#13 (Figure 1). Due to the x -dimension inconsistency of the sub-blocks, these MB#13 and SB#14 did not exactly align but did overlap approximately 10 mm with each other. As a result, we created a bump approximately 10 mm long of locally higher normal stress on a 760 mm long fault. The specific stress distribution caused by this bump is described in Figure 3 and Section 3.1.

A set of experiments were conducted at 2, 4, and 8 MPa $\bar{\sigma}_n$, with either zero shims, two shims (1.676 mm total thickness), four shims (3.353 mm), or six shims (5.029 mm). For each experiment we recorded a sequence of stick-slip events characterized by a sudden increase in the fault slip and a drop in $\bar{\tau}$. Each sequence contained five complete, sample-spanning, stick-slip ruptures. For each stick-slip event, we calculated $\bar{\tau}_p$, $\Delta\bar{\tau}_{\text{mech}}$, and $\Delta\bar{x}$, as shown in Figures 2a and 2b. The fault was considered to have reached “steady state” when those parameters were nearly identical for a sequence of at least five successive stick-slip cycles, and all results in this paper were taken after the fault reached steady state behavior. Figure 4 shows example sequences, and Figure 5 and Table 2 show all the experimental runs and their results.

2.3. Sensors and Data Acquisition

Apparent fault slip was measured at 0.15 μm precision using eight eddy current sensors (E1-E8) which measure the distance between a probe and target. The targets of each of the sensors were placed at 50, 140, 230, 320, 410, 500, 590, and 680 mm along the fault (Figure 1b). $\bar{\sigma}_n$ and $\bar{\tau}$ were measured with a precision of 1.5 and 0.73 kPa by hydraulic pressure sensors connected to hydraulic pistons (C1-C5) that applied load to the fault surfaces (Figure 1a). Four Panametrics V103 piezoelectric sensors attached with hot glue to the top of the blocks were used to measure vertical ground motion to within 0.3 mV. Two were attached to the MB 25 mm from the fault in the y -direction at 292 and 673 mm from the North end in the x -direction and two sensors were attached to the stationary block 25 mm from the fault at 127 and 534 mm from the North end. Data was continuously recorded at a rate of 50 kHz then averaged to 5 kHz on all sensors. The piezoelectric sensor data was also recorded in a triggered mode at 200 kHz.

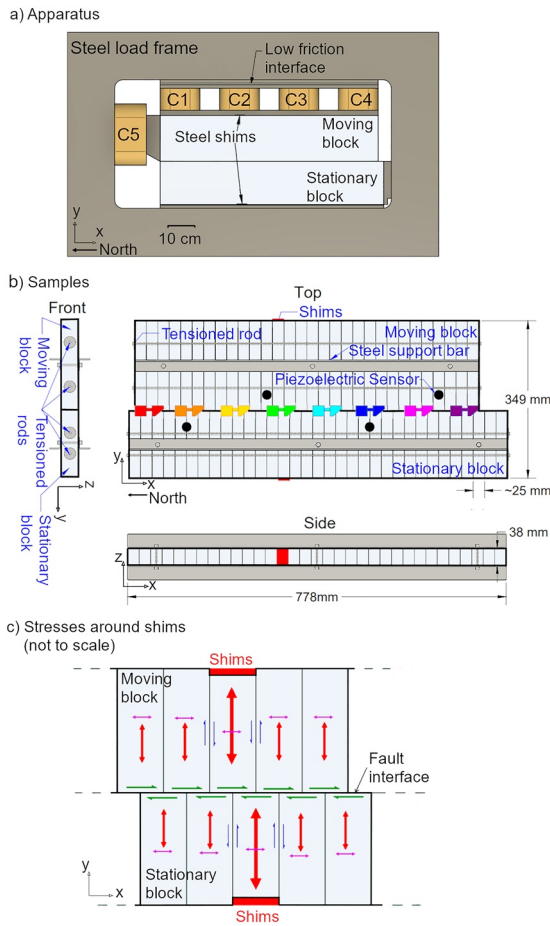


Figure 1. (a) Top view of the testing setup showing locations of the hydraulic cylinders, the sample, and the low friction interface. (b) Engineering schematic of the poly (methyl-methacrylate) composite specimen depicting shim placement, eddy current sensor and piezoelectric sensor locations along the fault, threaded tensioning rods that hold the sub-blocks together, and steel support bar. (c) Schematic of the sub-blocks with shims and neighboring sub-blocks similar to panel 1b top view (not drawn to scale). Arrows represent the stresses in individual sub-blocks as a result of applying $\bar{\tau}$ in the x -direction and $\bar{\sigma}_n$ in the y -direction. Size and direction of arrows indicate relative magnitude and direction.

The PMMA samples were painted with a speckle pattern near the fault to use for digital image correlation (DIC) (Appendix B, Figure 3.). The size of the speckles was chosen such that each speckle was approximately 2–20 pixels in the field of view chosen. A Nikon D850 camera with a pixel resolution of $8,256 \times 5,504$ was used to acquire images of the top of the sample to be analyzed with DIC. The camera was suspended so the lens was either 0.42 m or 0.98 m above the top of the sample and this provided a resolution of $37 \mu\text{m}/\text{pixel}$ or $90 \mu\text{m}/\text{pixel}$. In both cases the camera could detect individual speckles painted on the sample. The images were either taken manually with a remote or continuously every 1 s, so the sampling rate varied by experiment and is described in Section 3.1 and 3.4.2.

2.3.1. Apparent Slip Versus True Slip—Clarification of Slip Sensor Measurements

We refer to the displacement sensor measurements as “apparent slip” to distinguish between the displacement measured between the displacement sensor probe and target and the actual slip on the interface between the two samples. Because the sensor probe and target were offset in the x and y -directions, displacement sensor measurements were also somewhat sensitive to changes in shear strain. So, while displacement measurements show that the bump apparently slipped approximately $11.5 \mu\text{m}$ during small events (such as in Figures 6g and 6k), the DIC results (Figure 7) confirm that the bump did not slip and instead the apparent slip was the result of large increases in shear strain in that region.

A quick calculation can provide a rough sense of what order of strain changes can show up as apparent slip. The sensor probe and target were glued approximately 43 mm apart in the x direction and 16 mm apart in the y direction on the stationary and MB respectively. Based on a generalized Hooke's Law, $\Delta\tau = G * \frac{\Delta L_{xy}}{L_{xy}}$, an apparent slip of $\Delta L_{xy} = 11.5 \mu\text{m}$ over the sensor length of $L_{xy} = 46 \text{ mm}$ results in a strain increase of 2.5×10^{-4} . Given the compliance of PMMA ($G_{\text{PMMA}} = 1 \text{ GPa}$), this strain change converts to a stress change of 0.25 MPa. Considering the normal stress on the bump $\sigma_b = 37 \text{ MPa}$ during these experiments (Figures 3b, 6 shims at $2 \text{ MPa } \bar{\sigma}_n$), it is reasonable that a small slip event could result in a 0.25 MPa increase in shear stress on the bump, and that this shear stress increase accounts for the $11.5 \mu\text{m}$ of apparent slip. DIC, which can separate changes in shear strain from slip down to $3.7 \mu\text{m}$ (Appendix B), was used to confirm this discrepancy and shows cases where the bump did not slip, despite increases in apparent slip.

3. Results

3.1. The Effects of Shims on the Normal Stress Distribution

We define the increased normal stress of the bump above the sample average normal stress as $\Delta\sigma_b = \sigma_b - \bar{\sigma}_n$, as shown in Figure 3b. Based on generalized Hooke's Law, we roughly estimated $\Delta\sigma_{bt}$ using the equation:

$$\Delta\sigma_{bt} = \frac{E_{\text{PMMA}} * t}{L}, \quad (1)$$

where t is the thickness of the shims and L is the combined length of the stationary and moving blocks in the y direction. The steel shims are assumed to be infinitely stiff since their Young's modulus is much greater than

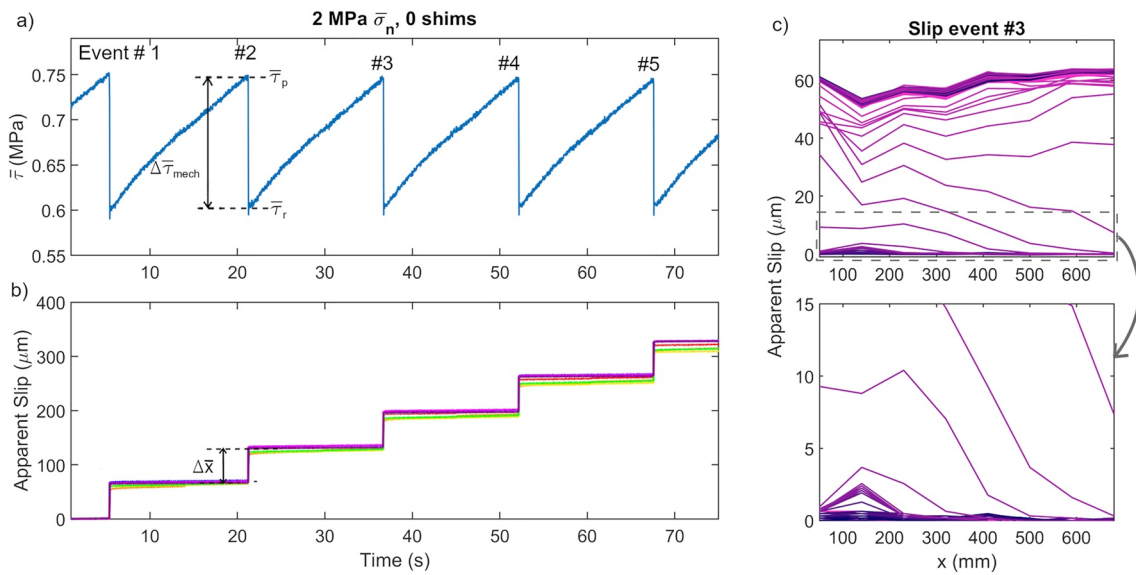


Figure 2. Example of a consistent sequence of stick-slip rupture events from Experiment 1 (2 MPa $\bar{\sigma}_n$, 0 shims). This figure points out key parameters used to compare stick-slip events. (a) $\bar{\tau}$ versus. time. (b) Apparent slip versus. time measured by displacement sensors for Experiment 1. Sensor colors correspond to the colors in Figure 1. Sudden decreases in $\bar{\tau}$ and increases in apparent slip indicate stick-slip events. (c) Apparent slip versus. space graphs for Event #3. Each line is plotted every 0.2 ms for a 0.2 s window centered at the start of the slip event. The colors cycle between pink and purple every 50 lines plotted. The lower panel shows the same data but zoomed in to show the rupture nucleation around $x = 150$ mm as indicated by the cluster of lines that show up to 3 μm of slip while other sections of the fault showed 0 μm of slip.

E_{PMMA} . Assuming values $E_{\text{PMMA}} = 2.6$ GPa (Kammer et al., 2012), $L = 349$ mm, and $t = 0.838$ mm/shim, we estimated $\Delta\sigma_{\text{bt}} = 12.5$ MPa for two shims, $\Delta\sigma_{\text{bt}} = 25.0$ MPa for four shims, and $\Delta\sigma_{\text{bt}} = 37.4$ MPa for six shims. According to this formulation, when the sample average normal stress is increased, the $\Delta\sigma_{\text{bt}}$ should remain constant since the number of shims added is constant. These experiments study $\Delta\sigma_{\text{bt}}/\bar{\sigma}_n$ from 0 to 18.7. We note that Equation 1 assumes frictionless behavior of the perpendicular faults between individual sub-blocks and uniform y -displacement of the entire sample (Figure 1c). When frictional interactions between adjacent sub-blocks are included, the stress increase on the fault may become more spatially distributed, with a smaller maximum $\Delta\sigma_{\text{bt}}$ (Figure 3b, $x = 315$ mm).

Benchmark tests with DIC were conducted to compare the experimental to theoretical normal stress distributions and are shown in Figure 3. In these benchmark tests, performed separately from experiments 1–12, the sample was loaded to prescribed $\bar{\sigma}_n$ with six shims in place. Photos were taken at each stress level for analysis using DIC. Figure 3a shows a sample image where purple boxes are annotations that mark correlation points used for the analysis. Correlation points were carefully chosen so that four points fall on each sub-block. Prior to this test, the sample had been loaded up to 8 MPa $\bar{\sigma}_n$ with no shims. The DIC stress measurements resolve normal stress to 5.6 MPa (see Appendix B for details) and clearly show the bump as a region of higher normal stress.

σ_b varied based on the $\bar{\sigma}_n$ and loading history. Higher $\bar{\sigma}_n$ resulted in higher σ_b . However, the higher σ_b was not erased by simply decreasing $\bar{\sigma}_n$. When loaded with shims, the sub-blocks slipped in the y -direction. This offset was held in place by a slight compression stress from the tensioned rods (See Appendix A for details). Overall, we see that $\Delta\sigma_b = \sigma_b - \bar{\sigma}_n$ measured with DIC roughly agrees with our theoretical estimate $\Delta\sigma_{\text{bt}}$ during the loading phase, so for simplicity we will use $\Delta\sigma_{\text{bt}}$ for comparison across experiments.

3.2. Typical Results

In all cases, the procedure outlined above produced a sequence of stick-slip events. We defined a stick-slip event as a sudden increase in apparent slip recorded by one or more displacement sensors with a minimum peak slip rate of 5 mm/s. In many cases, stick-slip events were coupled with a sudden decrease in $\bar{\tau}$ ($\Delta\bar{\tau}_{\text{mech}}$), as shown in Figure 2a. Figure 2 shows an example sequence of stick-slip events for Experiment 1 with the above parameters annotated. Figure 2b shows apparent slip as a function of time for eight displacement sensors. Figure 2c shows

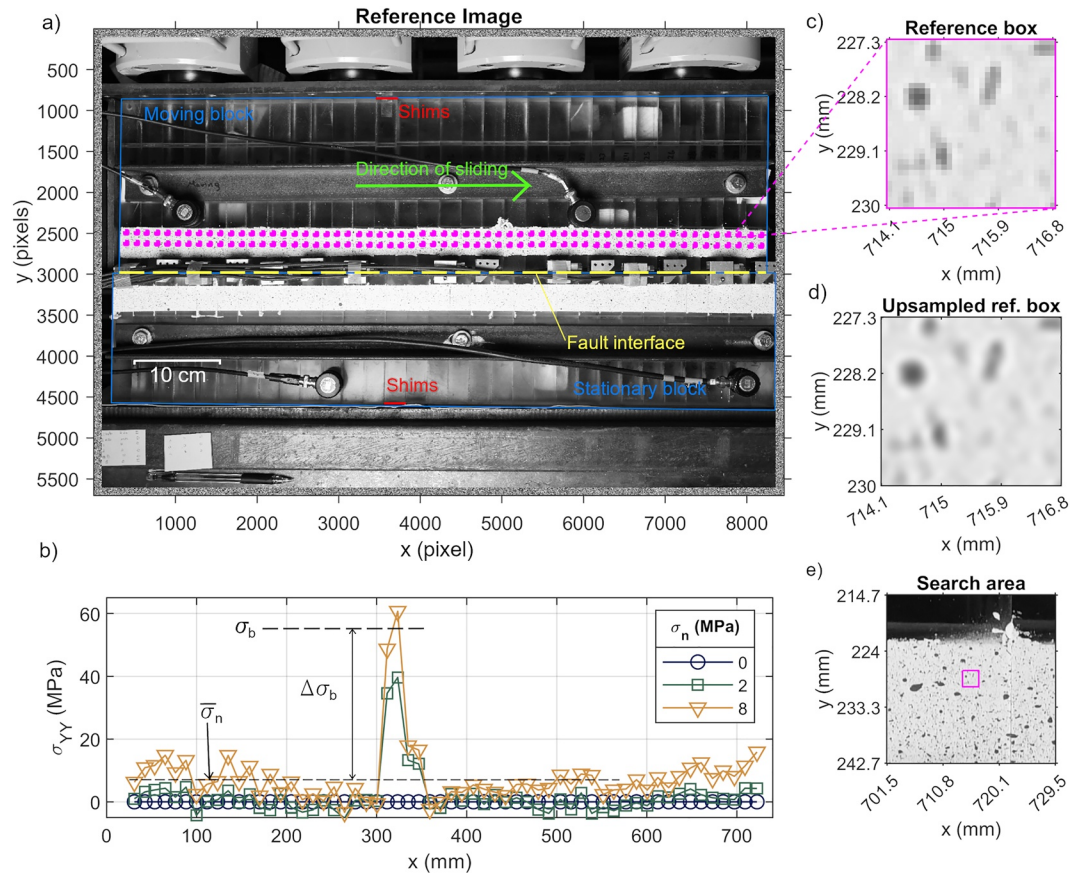


Figure 3. Digital image correlation (DIC) analysis of normal stress distribution of a bump created with six shims. (a) Example image used for DIC. Purple squares are annotations to indicate correlation points. Other details such as the shims, fault, and blocks are drawn to help orient the reader. (b) Normal stress as a function of distance along the fault for 0, 2, and 8 MPa $\bar{\sigma}_n$. (c) Example of the reference image (0 MPa $\bar{\sigma}_n$) box used to correlate across images. (d) Same reference box upsampled to 40 subpixels/pixel. (e) Example of search area used to correlate consecutive images (in this Case 2 MPa $\bar{\sigma}_n$) with the reference image.

the same slip sensor data in a 0.2 s window centered around Event #3 as a function of space. The top panel of Figure 2c shows the entire event, while the bottom panel shows a zoom in of the first 15 μm of slip to highlight the nucleation process. Cumulative apparent slip in this time window is plotted every 0.2 ms. Colors cycle from light pink to dark purple every 10 ms. Lines spaced far apart indicate fast, dynamic slip, while small distances between lines indicate slow slip or creep. Lines with a slope of zero indicate the fault has slipped uniformly, while sloped lines indicate one section of the fault has slipped more than others. The zoomed in panel of Figure 2c and indicates that slip began around $x = 150$ mm and propagated in the positive x -direction across the entire fault. At the end of the event, the fault had slipped 60 μm , mostly uniformly.

3.3. Overall Behavior of Sequences

We divide the observed sequences into two categories: consistent sequences and variable sequences. Consistent sequences produced slip events that always ruptured the entire sample in a series of complete-rupture instabilities, though there was often some variability in $\Delta\bar{x}$ and $\Delta\bar{\tau}_{\text{mech}}$ due to subtle variations in the rupture process. In these sequences, the bump slipped during every dynamic rupture event. Variable sequences contained at least one event where the bump remained unslipped. As such, variable sequences produced events with both partial and complete ruptures and therefore have more variable $\Delta\bar{x}$ and $\Delta\bar{\tau}_{\text{mech}}$ from event to event.

The two categories are illustrated by two representative sequences in Figure 4. Figure 4a is the consistent sequence from Experiment 1 (2 MPa $\bar{\sigma}_n$, 0 shims, $\Delta\sigma_{\text{bt}}/\bar{\sigma}_n = 0$), where each event slipped nearly the same amount

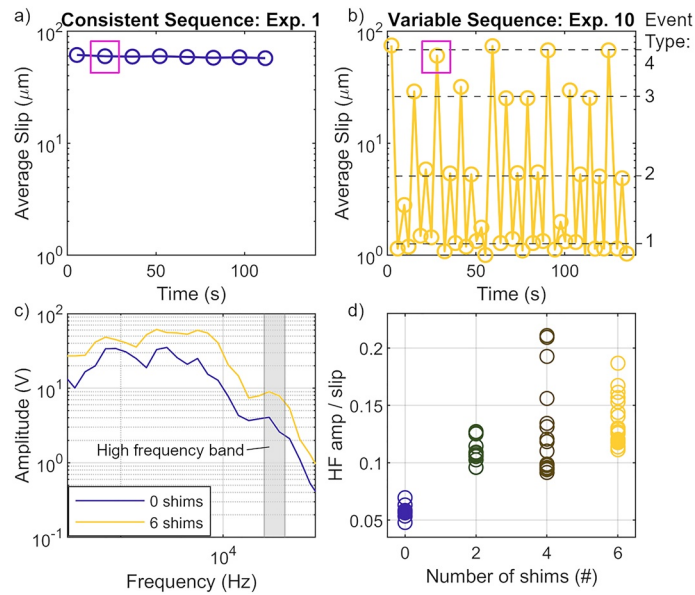


Figure 4. Comparison between a consistent sequence and a variable sequence and their radiated spectra. Average apparent slip versus time for (a) Experiment 1 (2 MPa $\bar{\sigma}_n$, 0 shims) and (b) Experiment 10 (2 MPa $\bar{\sigma}_n$, 6 shims) showing the sequences of events in the experiment. (b) also shows that events in (b) fall into four distinct levels of sample average slip. We group these events and label them as Types 1–4. (c) shows the spectra of events boxed in (a) and (b). Spectra were computed from the Fourier transform of 40 ms segments of recorded ground motions then averaged across the four piezoelectric sensors. The gray shaded region marks the high frequency band (28–35 kHz) used for comparison across experiments. (d) The ratio of the average high frequency amplitude (between 28 and 35 kHz) to average slip for each event in four experiments at 2 MPa $\bar{\sigma}_n$ with 0, 2, 4, and 6 shims. Filled in circles indicate the events analyzed in a–c.

(59.1 ± 2.2 μm) with a consistent recurrence time (15.2 ± 0.67 s). Figure 4b shows the variability of events in Experiment 10 (2 MPa $\bar{\sigma}_n$, six shims, $\Delta\sigma_{bt}/\bar{\sigma}_n = 18.7$). This sequence is characterized by frequent events (recurrence time of 3.07 ± 1.84 s) that can be categorized into four different types, based on the slip amount and location. Similar groupings can be made for other experiments with variable behavior.

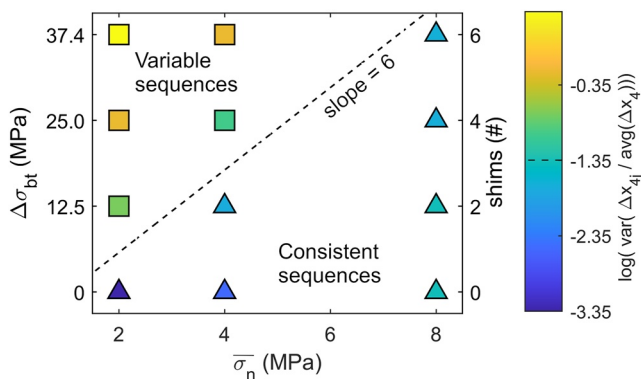


Figure 5. Map of the variability of laboratory earthquake sequences as a function of $\bar{\sigma}_n$ and $\Delta\sigma_{bt}$ (proportional to number of shims, as shown on the right y axis). Each marker indicates a different experimental run that generated a sequence of slip events; the color indicates the variance of the normalized average apparent slip. Triangles indicate consistent sequences (all complete rupture events, bump never stopped rupture) while squares indicate variable sequences (at least one partial rupture where the bump did not slip). The line with a slope of 6 (MPa/MPa) shows the separation between consistent sequences and variable sequences.

Sequences can also be characterized by the high frequency ground motions radiated by individual events. Figure 4c shows the amplitude of the Fourier transform of ground motions measured by piezoelectric sensors for two representative events from Experiments 1 and 10 (pink squares in Figures 4a and 4b). Ground motions from experiments with two and four shims follow a similar trend but were not shown, for clarity. To compare high frequency spectral amplitudes across many events, we used the average amplitude of the spectrum in the 28–35 kHz frequency band, shaded in gray in Figure 4c, normalized by event slip. Figure 4d shows this parameter and indicates that events from sequences with more shims showed more variability in radiated high frequency wave amplitude and produced, on average, more high frequency radiated energy compared to sequences with fewer shims.

Figure 5 presents a map of all 12 experiments in $\Delta\sigma_{bt} - \bar{\sigma}_n$ space. Squares denote variable sequences (bump stopped at least one rupture) and triangles are consistent sequences (bump never stopped rupture). More shims and lower $\bar{\sigma}_n$ resulted in variable sequences while fewer shims and higher $\bar{\sigma}_n$ resulted in consistent sequences. The boundary between the two sequence types corresponds approximately to a line with $\Delta\sigma_{bt}/\bar{\sigma}_n \approx 6$. However, our experiments cannot rule out a non-linear boundary in $\Delta\sigma_{bt} - \bar{\sigma}_n$ space. The $\Delta\sigma_{bt}/\bar{\sigma}_n \approx 6$ threshold is discussed further in Section 5.1.1. Near this boundary, there are

Table 2
Experimental Parameters From All Experimental Runs

Experiment #	$\bar{\sigma}_n$ (MPa)	Number of shims added	$\Delta\bar{x}$ (μm)			$\bar{\tau}_p$ (MPa)			$\Delta\bar{\tau}_{mech}$ (MPa)		
			Average	Min	Max	Average	Min	Max	Average	Min	Max
1	2	0	59	57	61	0.74	0.73	0.76	0.14	0.12	0.16
2	4	0	142	135	154	1.48	1.46	1.50	0.37	0.35	0.39
3	8	0	288	249	324	2.73	2.70	2.75	0.77	0.73	0.80
4	2	2	37	8	54	0.82	0.79	0.86	0.08	0.01	0.13
5	4	2	69	57	81	1.49	1.47	1.51	0.17	0.14	0.21
6	8	2	184	123	238	2.68	2.59	2.76	0.50	0.35	0.63
7	2	4	34	2	70	0.96	0.92	1.01	0.07	0.01	0.16
8	4	4	65	34	83	1.37	1.36	1.39	0.16	0.09	0.20
9	8	4	198	176	239	2.57	2.55	2.65	0.54	0.48	0.65
10	2	6	13	1	74	0.82	0.77	0.89	0.03	0.02	0.14
11	4	6	51	11	104	1.49	1.44	1.53	0.12	0.04	0.23
12	8	6	146	128	171	2.70	2.66	2.73	0.41	0.36	0.48

Note. Averages, max, and min are taken from sequences of events that included five complete stick-slip events.

some borderline cases such as Experiment 8 (4 shims, 4 MPa $\bar{\sigma}_n$) where only one of the eight events in the sequences did not rupture the entire fault.

The colors denote a quantitative measure of sequence variability based on the variance of the normalized apparent slip measured across the bump, $\hat{\Delta}x = \text{var}\left(\frac{\Delta x_{4j}}{\sum_{n=1}^k \frac{\Delta x_{4n}}{k}}\right)$, where Δx_{4j} is the apparent slip measured by the fourth eddy current slip sensor, located at $x = 320$ mm (target and probe span over the bump) during the j th event in the experiment and $\sum_{n=1}^k \frac{\Delta x_{4n}}{k}$ is the average apparent slip measured by the fourth eddy current slip sensor over all k slip events recorded in the experiment. $\hat{\Delta}x = 0$ means each event produced identical slip on the bump. A threshold of $\hat{\Delta}x = 10^{-1.35}$ cleanly separates consistent and variable sequences, shown as the dashed line in Figure 5. The boundary between consistent and variable sequences also marks a change in the behavior of $\hat{\Delta}x$. Variable sequences appear to become more variable (increasing $\hat{\Delta}x$) with distance from the boundary (moving toward the top left of Figure 5), while the variability of consistent sequences appears to primarily increase with increasing $\bar{\sigma}_n$ rather than distance from the boundary.

3.4. Sequence Details

3.4.1. Representative Consistent Sequence

Figure 2 shows Experiment 1 (0 shims, 2 MPa $\bar{\sigma}_n$, $\Delta\sigma_{bl}/\bar{\sigma}_n = 0$), which is a representative experiment where there is almost no variability among different events of the sequence. In consistent sequences, all rupture events typically initiated in the same location and slipped the entire fault uniformly, similar to Figure 2c.

3.4.2. Representative Variable Sequence

Experiment 10 (6 shims, 2 MPa $\bar{\sigma}_n$, Figures 6 and 7) had a prominent bump ($\Delta\sigma_{bl}/\bar{\sigma}_n = 18.7$) and weak surrounding fault ($\bar{\sigma}_n = 2$ MPa) and produced variable slip behavior. Figures 6a and 6b show $\bar{\tau}$ and apparent slip (colors correspond to the sensor locations shown in Figure 1) for the entire experiment and can be directly compared with Figures 2a and 2b. To understand this variable sequence, we consider both apparent slip and DIC measurements. Apparent slip, measured by displacement sensors which have a high temporal resolution and precision but low spatial resolution, is shown Figure 6. Slip measurements using DIC, which has a high spatial resolution (1.8 mm) but low temporal resolution (1 Hz) and precision (slip: 3.7 μm , τ : 1.4 MPa), are shown for a similar but not identical experiment also with 6 shims and 2 MPa $\bar{\sigma}_n$) in Figures 6g, 6k, and 7. DIC measurements focused on a 265 mm section of the fault centered around the bump. Images were taken at regular 1 s intervals. After experiments, an image before and after each slip event was selected for analysis. DIC slip measurements from

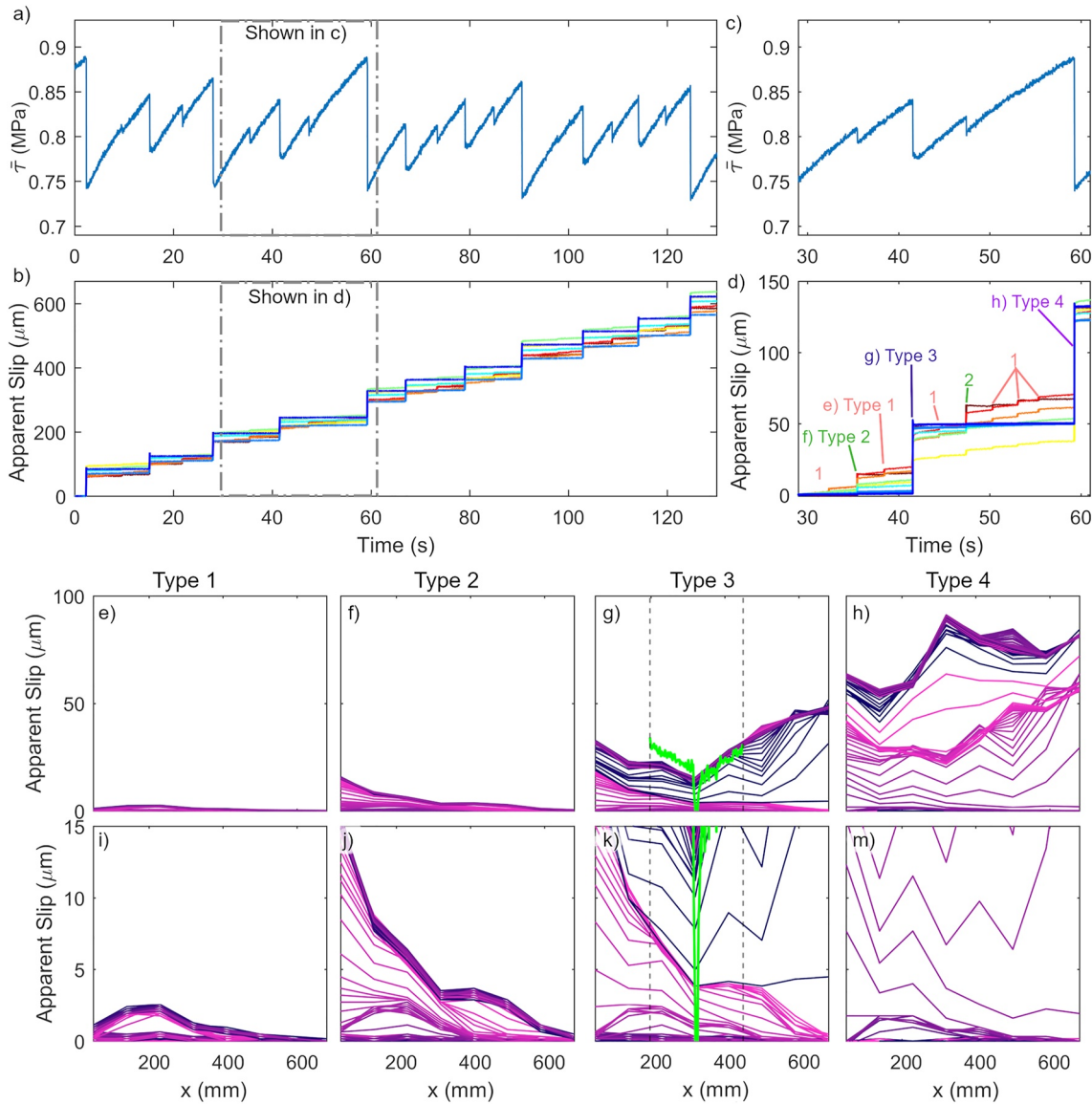


Figure 6. Example of a variable sequence. (a) $\bar{\tau}$ versus time for Experiment 10 (2 MPa $\bar{\sigma}_n$, 6 shims). Sudden decreases indicate stick-slip events that ruptured $x = 0$ mm. Stick-slip events that did not rupture $x = 0$ mm do not show up as a change in $\bar{\tau}$. (b) Apparent slip versus time measured by 8 displacement sensors. Colors correspond to the sensor colors shown in Figure 1c $\bar{\tau}$ for one supercycle. (c) Apparent slip, normalized at $t = 29$ s, for one supercycle sequence with Event types 1–4 indicated. (e)–(h) Apparent slip versus space graph of the events indicated in (d). Each line is plotted every 0.2 ms for a 0.2 s window centered on the start of the slip event. The colors cycle between pink and purple every 50 lines plotted. (i)–(m) Same events as shown in (e)–(h) but zoomed in on the y-axis to show initiation details. (g) and (k) also show slip measured from digital image correlation (which has higher spatial resolution and more accurate slip measurements) in a separate but similar experiment with $\bar{\sigma}_n = 2$ MPa and 6 shims, overlaid for reference. Light green line indicates slip and gray dashed lines indicate the field of view.

$x = 200$ – 300 mm and 350 – 450 mm (off the bump) are in good agreement with apparent slip measurements made by displacement sensors at approximately $x = 150$ and 450 mm during the same experiment as well as apparent slip measured during events in Experiment 10 (Figures 6g and 6k).

Rupture events in this sequence can be categorized into four main types (1, 2, 3, and 4) as seen in Figures 4b and 6e–6m, based on the amount and distribution of slip. The details of the four event types are specific to this experimental run, however all variable sequences displayed similar rupture partitions. Type 1 and 2 events were partial rupture events that only slipped a small portion of the sample, from $x = 0$ – 320 mm, and occurred most frequently during this experiment; Type 1 (Figures 6e and 6i) accounted for 55% of all slip events, Type 2 (Figures 6f and 6j) accounted for 20%. Type 3 events (Figures 6g and 6k) occurred less frequently (14%)

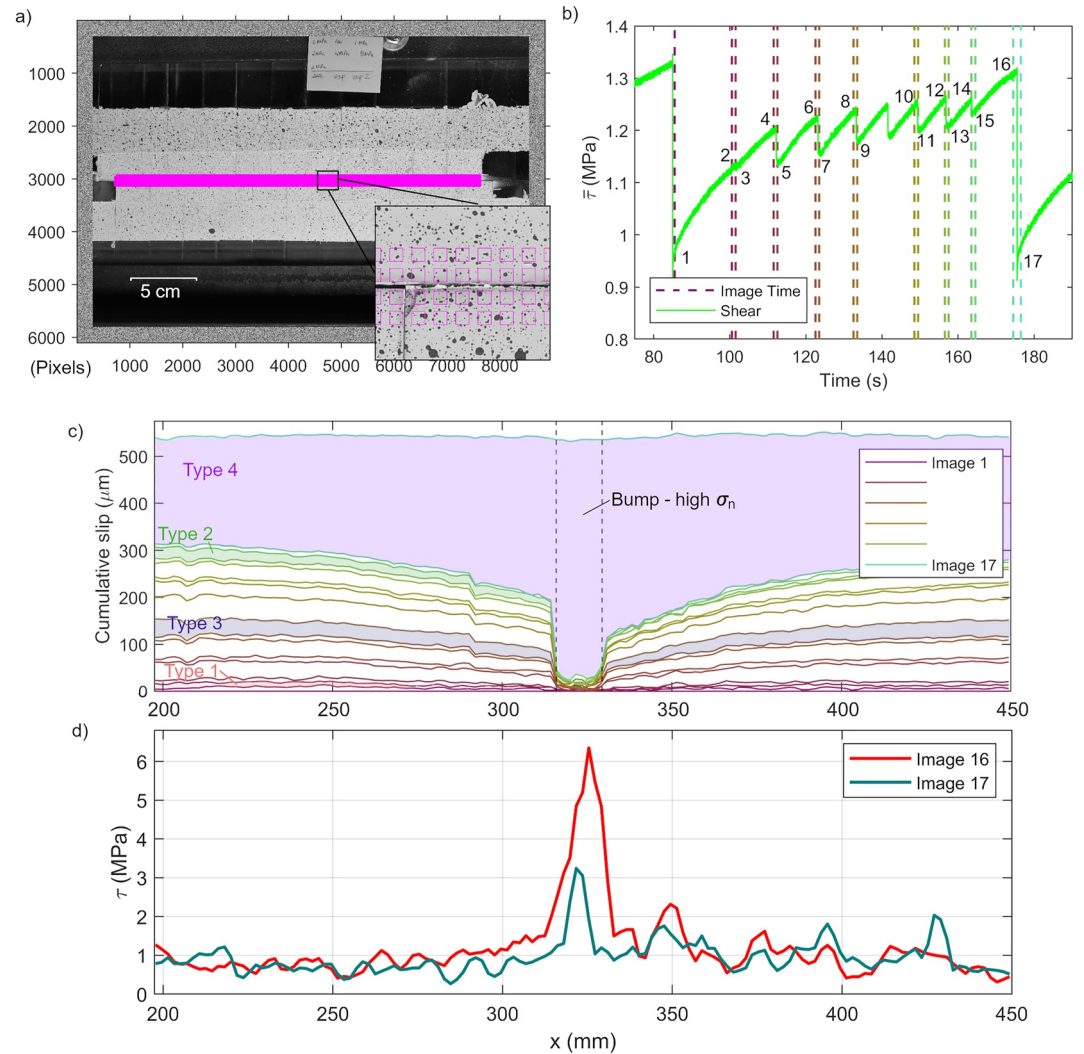


Figure 7. Digital image correlation (DIC) analysis of slip and shear stress on the bump during an experiment with 2 MPa $\bar{\sigma}_n$ and 6 shims (similar to Experiment 10). (a) Example image used for DIC. Purple boxes indicate correlation points. (b) $\bar{\tau}$ versus time to show the event timing relative to when images were taken. Sudden decreases in $\bar{\tau}$ indicate a stick-slip event. Images are taken at 1 s intervals throughout the experiment. Dashed lines indicate the images selected before and after most slip events that were used for analysis. Image 1 is used as a reference image for this analysis. Images are color-coded to match (c). (c) Cumulative slip derived from DIC for the series of images shown as a function of distance along the fault. One of each event type is shaded to show the slip in that event. Dashed black lines show the bump location. (d) Shear stress before and after the largest event derived from DIC measured approximately 1 mm from the fault for each image.

and slipped all of the fault except the bump. Type 4 events (Figures 6h and 6m) occurred least frequently (11%) and slipped the entire fault, including the bump. Larger rupture events always built upon smaller events (Figures 6e–6m). For example, Type 3 events first slipped as a Type 1 event, then continued as a Type 2 event, then continued to propagate. This is because all slip events nucleated around $x = 200$ mm (Figures 6e–6m) and is further discussed in Section 5.2.3. Type 4 and Type 3 events never occurred consecutively. A sample sequence that leads up to a Type 4 rupture can be seen in Figures 6c and 6d.

Type 1 events were very small ($\Delta\bar{x} \sim 1 \mu\text{m}$), as shown in Figure 6i. These events initiated around $x = 200$ mm and were contained between the North end ($x = 0$ mm) and the bump at $x = 320$ mm.

Type 2 events (Figure 6j) initially propagated as Type 1 events, then rupture paused for about 0.5 ms. The event then ruptured through the North end and slip accelerated there, likely due to the free surface at $x = 0$ mm. This caused rupture to propagate back along the sample. The eddy current displacement sensor data shows an increase

in apparent slip on the bump; however, DIC (Figure 7) shows that the bump remained locked. Beyond the bump, apparent slip increased, but the rupture did not slip through the leading end at $x = 760$ mm.

Type 3 events ($\Delta\bar{x} \sim 30 \mu\text{m}$, shown in Figures 6g and 6k) initially propagated as a Type 2 event. The event paused for 1 ms, and then ruptured through the South end of the sample at $x = 760$ mm. Slip acceleration on the sample end, likely caused by the ruptured free surface, which caused a back propagation of rupture through the entire sample (except the bump which remained locked, described below). Compared to eddy sensor measurements, slip measured with DIC has higher spatial resolution and is closer to the true fault slip. DIC slip measurements between images 8 and 9 (Figure 7b), plotted with a green line in Figures 6g and 6k, are in agreement with the slip off the bump ($200 \text{ mm} < x < 315$ and $330 \text{ mm} < x < 450$ mm) but show that the bump slipped $1.7 \mu\text{m}$. However, the DIC noise level is $3.7 \mu\text{m}$ (Appendix B) so likely the bump remained locked and the measured slip is noise. The bump remained locked and the increase in apparent slip in Figures 6g and 6k is caused by an increase in shear strain (Section 2.3.1).

Type 4 events initially ruptured as a type 3 event, paused, and then slip initiated on the bump. In event Types 1–3, the bump acted as a barrier, however in Type 4 events, the bump acted as an asperity. As an asperity, the bump slipped significantly more compared to the rest of the fault, and relieved the built-up slip deficit (Figure 7c) characteristic of Type 4 events. When the bump slipped, it also reruptured the previously slipped regions of the fault, which resulted in a slip event that was larger than Type 1–3 events or events without shims (Figure 4).

The DIC analysis also allowed us to measure the changes in $\tau(x)$ on the bump (Figure 7d) to within 1.4 MPa. τ measurements outside the bump at $\bar{\sigma}_n = 2$ MPa are near our minimum resolution (0.47 MPa, Appendix B) and noise level (1.4 MPa, Appendix B), so changes are generally too small to resolve. Smaller stress bumps (e.g., at $x = 350$ mm, 377 mm, 427 mm) are due to shear stress irregularities due to the sub-blocks of the composite sample (See Appendix A). With consecutive small events, $\tau(x)$ on the bump gradually increased while the bump remained locked. $\tau(x)$ reached a peak of about 6 MPa in image 16 (lighter red line) just before the bump slipped. After the bump slipped, image 17 (darker blue line) shows a much lower $\tau(x)$, ~ 3 MPa, and the area of increased $\tau(x)$ also decreased spatially.

To summarize, in event Type 1, the bump acted as a barrier, remained locked and prevented rupture propagation which limited the rupture size. In event Types 2 and 3, the bump remained locked and acted as a barrier, however it was not able to stop rupture. Even though the bump presumably extended the full depth of the sample (38 mm in the z direction), the bump was effectively by-passed due to stress changes ahead of the rupture front. In this case, a Type 2 event provided a large enough stress increase beyond the bump at $x = 400$ mm for rupture to reinitiate there. Only in rupture Type 4 did the bump eventually act as an asperity and unload the built-up stress from several Type 1–3 events.

3.4.3. Spectral Analysis

Spectral analysis of the ground motion signals recorded from the piezoelectric sensors in experiments with $\bar{\sigma}_n = 2$ MPa (Experiments 1, 4, 7, and 10 with 0, 2, 4, and 6 shims) show that increased shims increased high frequency radiation (Figures 4c and 4d). Spectra were computed by taking Fourier transforms of 40 ms windows of piezoelectric sensor signals. Spectra from the four sensors were averaged to produce a more stable estimate across events, then the Fourier frequency estimates were averaged into log-spaced frequency bins for clarity. We compared the average amplitude in the 28–35 kHz frequency band (gray shaded area in Figure 4c) normalized by the average apparent slip across events and experimental runs. This frequency band was chosen since it is above the expected corner frequency of all events (~ 100 – $1,000$ Hz) and still had ample signal-to-noise ratio for all events studied. Two events from Experiment 4 and one event from Experiment 10 were not well centered in the recorded triggered window and were disregarded in the analysis.

4. Summary of Key Observations

From the above results the key observations are:

- (1) Smaller bump prominence ($\Delta\sigma_{\text{bt}}/\bar{\sigma}_n < 6$), due to fewer shims or higher $\bar{\sigma}_n$, promoted consistent rupture sequences with periodic and nearly identical stick-slip events (Figure 2)

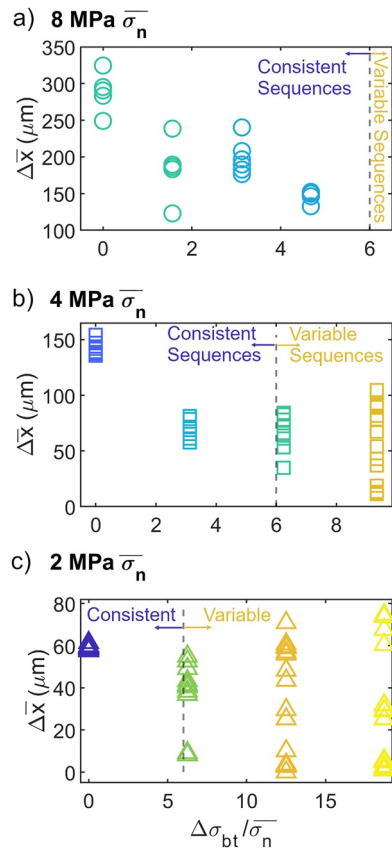


Figure 8. Sample-average slip versus bump prominence for (a) 8 MPa, (b) 4 MPa, and (c) 2 MPa $\bar{\sigma}_n$. Each marker indicates an individual stick-slip event and colors for each experiment match those in Figure 5. Vertical dashed lines indicate $\Delta\sigma_{bt}/\bar{\sigma}_n = 6$. Data points to the left of that line indicate experiments with subcritical bumps that never stopped ruptures.

- (2) Larger bump prominence ($\Delta\sigma_{bt}/\bar{\sigma}_n \geq 6$), due to more shims or lower $\bar{\sigma}_n$, promoted variable sequences with both partial- and complete-rupture events in the same sequence with the same loading conditions.
- (3) The different sized events described in (2) occurred because either:
 - a) The bump acted as a barrier and completely stopped rupture (e.g., Type 1 events, Figures 6i and 7c).
 - b) The bump acted as a barrier but was by-passed such that slip re-initiated beyond the bump (e.g., Type 2 and 3 events, Figures 6k and 7c).
 - c) Rupture initiated elsewhere but caused the bump to slip and release a large amount of shear stress. The bump acted as an asperity and this resulted in a larger rupture than otherwise expected (e.g., Type 4 events, Figures 6l, 7c, and 8).
- (4) In variable sequences, the larger ruptures always built upon the smaller ruptures. For example, rupture Type 2 began in an identical fashion to rupture Type 1, paused near the termination of rupture Type 1, but then ruptured further. Similarly, rupture Type 3 began in an identical fashion to rupture Types 1 and 2, paused, and then it ruptured beyond the final rupture of Type 2.
- (5) The pauses described in (4) ranged from 0.3 to 1 ms.
- (6) The variability of the sequences persisted even after the bump had ruptured multiple times.

5. Discussion

These experiments present complex, variable rupture sequences on an approximately 1D fault created simply by adding a localized region of increased normal stress (a bump). Compared to experiments on a more homogenous fault ($\Delta\sigma_{bt}/\bar{\sigma}_n < 6$), a more prominent bump ($\Delta\sigma_{bt}/\bar{\sigma}_n > 6$) promoted partial rupture events and large variability in event sizes.

In the variable sequences, the sample was loaded at a constant rate, and all earthquakes initiated in the same location (described in more detail in Section 5.2.3). The variations in earthquake sizes that we observed are

entirely the result of differences in dynamic rupture propagation and arrest. These differences resulted from variable initial shear stress conditions. For example, one earthquake might not quite make it past the bump and would terminate. This increased shear stress on the bump. The very next dynamic rupture event of a sequence might start similarly but rupture through the previously stressed bump and continue to grow into a larger rupture. In the first rupture, the bump acted as an energy sink or a barrier. Instead of strain energy driving rupture propagation, it went into an increase in shear stress on the bump. In the second rupture, the strain energy was sufficient to push the stress on the bump above some critical threshold and the stored strain energy from the first rupture was released. In this case, the bump acted as an asperity. Thus, the addition of a bump can cause the same section of a fault to sometimes produce a small earthquake and sometimes produce a large earthquake. This variable bump behavior is similar to an earthquake gate and can persist over many seismic super cycles (Duan et al., 2019; Oskin et al., 2015; Rodriguez Padilla et al., 2022).

We note that our experiments are a simplified case where rupture always initiated at the same location and there was only one normal stress bump and the two free ends of the sample that also acted similar to bumps. In a more complex system where events can nucleate in multiple locations or where more bumps are involved, there will be a larger variation in event size and location. However, the rupture behavior observed in our simplified experimental system over many stick-slip cycles provides insights into the dynamics of complex ruptures.

5.1. Conditions for Barrier-Like Behavior

Whether or not a bump can stop a rupture depends on the amount of shear stress transferred to the bump by the nearby rupture and the bump's strength excess, $\tau_p - \tau_0$, which is its ability to accommodate additional shear stress without slipping (Boatwright & Quin, 1986). Utilizing fracture mechanics solutions for the elastic stress field around a crack tip (Zehnder, 2012, Equations 2.82 and 2.95) we find a linear relationship between the stress increase a distance r ahead of the crack tip, and the stress drop ($\tau_0 - \tau_r$) within the shear crack of half-length a ,

$$\Delta\tau(r) = \frac{(\tau_0 - \tau_r)\sqrt{\pi a}}{\sqrt{2\pi r}}, \text{ for } r > a. \quad (2)$$

Larger stress drops within the rupture region result in a larger shear stress increase at the crack tip. For the bump to act as a barrier, the stress increase from the rupture, must be less than the bump strength excess. Slip events that have a larger local stress drop, require a bump with higher strength excess to stop the rupture.

This agrees with our experimental observations that show that at lower $\bar{\sigma}_n$, fewer shims were needed to stop some ruptures and produce variable sequences (Figure 5). In contrast, higher $\bar{\sigma}_n$ resulted in higher local stress drops during rupture events and therefore higher stress increase outside the ruptured region. For example, Experiment 3 (0 shims, 8 MPa $\bar{\sigma}_n$) had an average $\Delta\bar{\tau}_{\text{mech}}$ of 0.77 MPa and Experiment 1 (0 shims, 2 MPa $\bar{\sigma}_n$) had an average $\Delta\bar{\tau}_{\text{mech}}$ of 0.14 MPa (Table 2). A larger bump (more shims) with larger strength excess was needed to stop those higher stress drop events.

5.1.1. Threshold Prominence $\Delta\sigma_{\text{bt}}/\bar{\sigma}_n$ to Stop Rupture

We found the criteria $\Delta\sigma_{\text{bt}}/\bar{\sigma}_n \approx 6$ as an approximate cutoff between consistent behavior and variable behavior (Figure 5) as defined in Section 3.3. We compare our results to the modeling study of Sudhir (2022), who explored a 2D interface governed by rate-and-state friction with multiple normal stress bumps. Sudhir (2022) considered the maximum normal stress on the bump, $\sigma_b = \Delta\sigma_b + \bar{\sigma}_n$ (Figure 3) rather than $\Delta\sigma_b$, so we relate our observations to hers using $\frac{\Delta\sigma_{\text{bt}}}{\bar{\sigma}_n} = \frac{\sigma_b - \bar{\sigma}_n}{\bar{\sigma}_n} = \frac{\sigma_b}{\bar{\sigma}_n} - 1$. She also found a threshold $\Delta\sigma_{\text{bt}}/\bar{\sigma}_n \approx 6$ that separated sequences with only system-spanning events from those that sometimes produced isolated small-scale ruptures (i.e., foreshocks) via localized slip of the bumps. Both Sudhir (2022) and our experiments suggest that $\Delta\sigma_{\text{bt}}/\bar{\sigma}_n \geq 6$ is required for a bump to remain unslipped despite slip on the surrounding fault. However, different from our experiments, Sudhir (2022) studied multiple bumps on a 2D fault, rather than one bump on our largely 1D interface and her bumps remained unslipped despite slow and accelerating slip on the surrounding interface rather than dynamic slip as in our case. We expect that bumps with higher $\Delta\sigma_{\text{bt}}/\bar{\sigma}_n$ are required to stop rupture in the 2D case, due to the geometrical intensification of stress associated with slip “wrapping around” a bump in 2D. In contrast, slow slip events typically have lower stress drop and would therefore be stopped by bumps with smaller $\Delta\sigma_{\text{bt}}/\bar{\sigma}_n$ than fully dynamic slip events with larger local stress drop. The interaction of these two competing factors may produce a similar $\Delta\sigma_{\text{bt}}/\bar{\sigma}_n$ threshold despite differences between our experiments and the models of Sudhir (2022).

Regardless of the specific value of the $\Delta\sigma_{\text{bt}}/\bar{\sigma}_n$ threshold, we believe the existence of such a threshold makes sense theoretically if we consider the balance of stress at the crack tip and bump strength excess. Based on Equation 2, stress increase on the bump will primarily depend on the stress drop in the ruptured region, which is arguably proportional to $\bar{\sigma}_n$, via friction parameters. Similarly, the strength excess on the bump is arguably proportional to $\Delta\sigma_{\text{bt}}$, again, via friction parameters. Appendix C presents an analogy that is helpful to understand why $\Delta\sigma_{\text{bt}}/\bar{\sigma}_n$ affects whether a bump stops rupture or not. Therefore, the ratio $\Delta\sigma_{\text{bt}}/\bar{\sigma}_n$ is a reasonable parameter to determine if a nearby rupture will always propagate through a bump or if, under some initial shear stress conditions, the bump may stop rupture. Our proposed threshold of $\Delta\sigma_{\text{bt}}/\bar{\sigma}_n \approx 6$ is approximate, but because it is primarily dependent on frictional constants, we believe that it may be a universal feature of faults at a variety of scales and expect this to remain relatively constant throughout much of the seismogenic crust.

There are, however, some caveats to the above argument. In our experiments, ruptures interact with a barrier that is much larger than the cohesive zone size (estimated $<100 \mu\text{m}$). Barriers may affect rupture differently if fault weakening occurs over larger spatial scales. Also, enhanced weakening (e.g., Di Toro et al., 2011) that significantly increases $(\tau_0 - \tau_r)$ near the rupture tip could also modify the proposed threshold. Finally, characteristics of the stress increase at and ahead of the rupture tip may be affected by the total crack size (a in Equation 2), and

this may be an area for continued research. Our experiments exhibit relatively well developed ruptures that likely propagate close to the Rayleigh wave velocity and have rupture lengths that are long compared to the nucleation length, and in this regime we might expect the dependence on a to be weak. While Equation 2 can serve as a rough guide, its precise application to a propagating shear rupture is not entirely straightforward. For example, a pulse-like rupture would not scale with a , and simulations of crack-like ruptures that employ a slip-weakening friction relation also do not show a significant scaling of stresses near the rupture tip with overall rupture length (Ke et al., 2022).

5.2. Variable Sequences

Experimental runs with more shims and lower $\bar{\sigma}_n$, that is, with $\Delta\sigma_{bt}/\bar{\sigma}_n > 6$, resulted in complex sequences where slip events varied with regard to slip amount, rupture length, and slip rate (Figure 6). More shims created a larger $\Delta\sigma_{bt}/\bar{\sigma}_n$ and a more heterogeneous $\tau_p(x)$. Some patches on the fault had low strength and slipped with a short recurrence time, while the bump had far higher strength. This resulted in sequences where several small events occurred between each large event and large events never occurred consecutively, similar to the “barrier-type” events proposed by Aki (1984). Each small event increased shear stress on the bump until stress levels reached a critical state and the bump slipped.

5.2.1. Bump Slips (e.g., Type 4 Event)

When the bump did finally slip, it released a large amount of the built-up strain energy in a complete-rupture event that was larger than those produced without a bump. Because the bump was near critically stressed, the small elastic stress change from rupture elsewhere on the fault was sufficient to initiate slip on the bump and unlock the stored strain energy in the bump. This is similar to natural observations of large earthquakes that relieve built up strain or slip deficit. Herman et al. (2018) used a simple asperity model to model a slip deficit prior to the 2011 Tohoku earthquake. During the earthquake, the slip deficit was relieved which released a large amount of stress and started a chain reaction of other asperities. Similarly, earthquake gates can terminate very large ruptures, but can also allow ruptures to pass through and grow even larger (Duan et al., 2019; Rodriguez Padilla et al., 2022).

In our experiments, we measured a larger local stress drop $\Delta\tau$ on the bump ($x = 320$ mm) than elsewhere on the fault (Figure 7d, compare Image 16 to Image 17). For a critically stressed fault patch $\Delta\tau = (\mu_s - \mu_d) * \sigma_n$, where $(\mu_s - \mu_d)$ is the difference between a static and dynamic coefficient of friction. Since the bump has a higher σ_n , $\Delta\tau$ is larger than the rest of the fault. In short, high σ_n bumps can produce large local stress drops if they are critically stressed. After the bump slipped, the stress on the bump was greatly reduced, the bump's strength excess was high, and the bump then acted as a barrier or energy sink for subsequent events.

The large local stress drop $\Delta\tau$ associated with slip on the bump caused stress redistribution that promoted a large amount of slip elsewhere on the fault and resulted in a large sample-average stress drop $\Delta\bar{\tau}_{mech}$. However, we cannot link measured $\Delta\bar{\tau}_{mech}$ to seismological stress drop because the free edges at the ends of the laboratory fault differ from the boundary conditions of natural earthquakes. Steinhardt et al. (2023) found that seismological stress drop was independent of normal stress for fully confined slip events, and Schaal and Lapusta (2019) similarly found that high normal stress bumps did not produce abnormally high seismological stress drops when they ruptured. This is likely because the locally higher stress drop on a bump will be offset by further rupture propagation into unfavorably stressed regions, resulting in a rupture-averaged stress drop that is more modest.

5.2.2. Rupture By-Passes the Bump (e.g., Type 3 Event)

One potentially important outcome was ruptures that terminated at the bump and then initiated as a separate rupture on the other side of the bump while the bump remained locked. This is the same as the case of a rupture “skipping past” a barrier, described by Das and Aki (1977), except that their simulations allowed for instantaneous rupture initiation on the other side of the barrier, and our experiments show a time delay related to the re-nucleation process. Our observations are very similar to the termination and nucleation processes observed near a barrier of high fracture energy by Gvirtsman and Fineberg (2021) who saw that even though rupture terminated at the barrier, the elastic stress redistribution could trigger slip on the fault beyond the barrier. They matched the measured shear stress changes after the rupture terminated at the barrier to the fracture mechanics predicted stress singularity and the time delay between termination of the previous rupture and initiation of a new rupture. Different from the earlier studies, we also observed cases where the

second rupture then propagated backward along the fault and reruptured sections of the fault that had recently (<5 ms earlier) slipped. In our simple experimental setup, we do not consider variations in speed or size of the terminated event as Gvirtsman and Fineberg (2021) did, so their study may offer helpful insights to link these experiments to more complex systems. Importantly, for such a rupture bypass to occur, the stress concentration at the rupture front does not drive rupture; rather, the much more modest stress increase ahead of the rupture front does.

Since $\Delta\tau(r)$ decreases ahead of the crack tip (Equation 2), this introduces a spatial scale that was not addressed here or in Gvirtsman and Fineberg (2021). Caniven et al. (2017) studied a spatially larger, but lower amplitude normal stress asperity. While they observed a similar rupture partitioning as in this study, they did not observe any cases where the rupture by-passed the bump, likely because the low rigidity of their model material caused very small $(\tau_o - \tau_p)$ in Equation 2 and this resulted in small $\Delta\tau(r)$.

The re-nucleation component mentioned above also adds some additional variability into the rupture process. Earthquake nucleation has been shown to be extremely sensitive to small details such as the fault “state” (i.e., how healed it is) as well as loading rate, heterogeneity, and other processes (McLaskey, 2019). If an earthquake's multi-phase dynamic rupture process also includes nucleation within it, this potentially makes the rupture process far more susceptible to variation due the above-mentioned details.

5.2.3. Variability in Sequences Dictated by Initial Stress Conditions

Despite large variations in event size, all events in variable sequences initiated at the same location along the fault where $\tau_p(x)$ was a minimum. For example, in Experiment 10 (6 shims, 2 MPa $\bar{\sigma}_n$, shown in Figure 6) all events initiated at approximately $x = 220$ mm. The benchmark stress test in Figure 3b, also showed that $\sigma_n(x)$ was lowest from $x = 200$ –280 mm. Assuming $\tau_p = \mu_s \sigma_n$, this suggests that the fault is weakest (lowest $\tau_p(x)$) at this location. With an approximately uniformly distributed increase in shear stress along the fault, slip will commence at the weakest location. We believe $\sigma_n(x)$ and frictional properties remain constant throughout an experiment. Consequently, $\tau_p(x)$ remains constant as well and that controls the initiation location.

Given that all events initiated at the same location, the variations in event size within a sequence are due to variations in $\tau_0(x)$. This has been shown in previous studies (Bayart et al., 2018; Cebry, Ke, & McLaskey, 2022; Kammer et al., 2015; Ke et al., 2021) where rupture size is limited by the area of the fault that is favorable for propagation. Ruptures that propagate into an unfavorably stressed region terminate. This effect combined with a persistent normal stress heterogeneity, provides a means for complex sequences with distinct individual ruptures, such as those observed in Experiment 10. Rupture types with many phases were always triggered by elastic stress redistribution from the earlier phases of rupture, and whether or not the elastic stress change from an earlier rupture phase was sufficient to initiate the next phase of rupture depended on $\tau_0(x)$ prior to rupture. Models by Cattania and Segall (2021) with more realistic variations in normal stress showed similar variation of event sizes. Even with normal stress variations longer than the nucleation length, low normal stress areas slipped stably early in the modeled earthquake cycle and loaded locked high normal stress areas which eventually slipped seismically. In our simple experiment, and in more complex systems, the details of the initiation process were not sufficient to predict the eventual size of the event. Knowledge of the strength and stress state ($\tau_p(x)$ and $\tau_0(x)$, respectively) was required.

5.3. Effect of a Subcritical Bump, $\Delta\sigma_{bt}/\bar{\sigma}_n < 6$

While bumps with $\Delta\sigma_{bt}/\bar{\sigma}_n < 6$ may not be sufficient to stop ruptures, they still had an effect on the resulting slip event. Figure 8 shows $\Delta\bar{x}$ for individual events in each experiment as a function of bump prominence. More prominent subcritical bumps tended to reduce $\Delta\bar{x}$. For example, $\Delta\bar{x}$ decreased from 288 μm in Experiment 3 (0 shims, 8 MPa $\bar{\sigma}_n$) to 180 μm in Experiment 6 (2 shims, 8 MPa $\bar{\sigma}_n$). One possible reason for this is that we applied a constant $\bar{\sigma}_n$ which is the average of both the bump and the regions outside the bump. A larger bump increased σ_b , but since $\bar{\sigma}_n$ remained constant, $\sigma_n(x)$ off the bump decreased. As a result, the majority of the fault acted as if $\bar{\sigma}_n$ was lower, that is, it reached a critical stress more quickly, and upon rupture produced a smaller $\Delta\tau$ and therefore, less slip. On the other hand, beyond the threshold of $\Delta\sigma_{bt}/\bar{\sigma}_n = 6$ (i.e., to the right of the vertical dashed lines), more variability was observed and the size of the largest events sometimes increased beyond that of experiments without a bump.

5.4. Effect of the Bump on Earthquake Spectra

Figures 4c and 4d show spectral analysis of events in experiments conducted at 2 MPa $\bar{\sigma}_n$. An increase in shims increased the amount of high frequency seismic radiation (28–35 kHz band) when normalized to average apparent slip, which should be proportional to seismic moment. This high frequency band was chosen because it is clearly above the events' expected corner frequency (~ 100 – $1,000$ Hz). Sample-spanning or near sample-spanning events that occurred despite a prominent bump, such as Type 3 and 4 events in Experiment 10, sped up and slowed down multiple times during the event. These stops and restarts likely emitted more high frequency seismic waves than a continuous rupture front, as suggested by numerical modeling (Das & Aki, 1977; Dunham et al., 2011; Oral et al., 2022; Shi & Day, 2013). This is relevant for natural faults from a seismic hazard perspective, as rupture of heterogeneous faults can amplify the high frequency seismic waves (above the corner frequency) that typically damage man-made structures.

Our experimental setup lets us observe rupture details that are likely not resolvable in larger natural earthquakes using the tools of seismology. For example, without the spatial and temporal resolution of the laboratory measurements made with slip sensors and DIC, the complex set of ruptures illustrated in Type 4 events (Figure 6h) may appear as one single rupture that simply slowed down when it encountered a bump and potentially sped up after passing it. For natural earthquakes, such speedups and slowdowns have been observed with back projection imaging (e.g., Bao et al., 2022). A more complete consideration of the seismic implications of rupture interactions with a bump is the topic of a future study.

5.5. Creeping Faults and Inelastic Processes

The experiments presented here only slipped in sequences of dynamic stick-slip events. The critical nucleation length h^* is likely small, <10 – 100 mm (Cebry & McLaskey, 2021), so all events were dynamic stick-slip events, and the effects of creep or slow slip were not observed. Creep or slow slip on natural faults can elastically redistribute shear stress similar to the way the smaller dynamic events did in the current experiments (Cebry, Ke, & McLaskey, 2022; Herman et al., 2018; Lay et al., 2012). We can think of a hypothetical situation where a large creeping patch is located next to a high-strength bump. The bump may have sufficient strength to stop consecutive slow slip events, but over time the bump's strength excess will be reduced and eventually it will fail as a result of nearby slow slip or an incoming large dynamic event (Cattania & Segall, 2021).

Another complicating factor of natural faults is inelastic processes which may act to reduce the stored shear stress on the bump during the interevent periods. Similar to observations of a restraining stepover, a bump may remain locked during a dynamic rupture, but over time, fractures and other damage processes in the surrounding area could relieve a fraction of the stress built-up on the bump (Dunham et al., 2011; McClay & Bonora, 2001). This would allow the bump to regain some strength excess with time. These inelastic processes, not clearly observed in the current experiments, may modify the mechanics of how bumps behave in natural fault systems.

6. Conclusion

Laboratory experiments on a unique sample with a central bump of high normal stress resulted in varied slip behavior. Without a bump (i.e., no shims added), the sample had a nearly uniform distribution of normal stress and produced sequences of highly periodic and nearly identical complete-rupture stick-slip events. The addition of a localized bump of high normal stress of sufficient prominence ($\Delta\sigma_{bt}/\bar{\sigma}_n > 6$) in the center of the sample produced frequent, smaller, partial rupture events and occasional, larger, complete rupture events, even under identical, constant loading conditions. We found that a bump with sufficient strength excess (due to low τ_o and/or high τ_p) acted as a barrier that stopped ruptures. However, a bump never acted as a permanent barrier. Partial rupture events (i.e., events that were stopped by a bump) incrementally increased the shear stress on the locked bump and accumulated until the bump became critically stressed and eventually rupture propagated through the bump. This process was imaged using DIC, shown in Figure 7. When the bump finally slipped, it acted as an asperity. The built-up stress was released in a complete-rupture event that could be larger than those produced without a bump. Our experimental observations corroborate with the descriptions of Aki (1984): when the bump behaves as a barrier it roughens the shear stress distribution, and when it slips as an asperity it smooths the stress. The addition of a bump can cause the same section of a fault to sometimes produce a small earthquake

and sometimes produce a large earthquake, and unlike heterogeneity in initial stress, the bump and its variable behavior can persist over many seismic super cycles.

Experiments with few shims or high sample-average normal stress, $\bar{\sigma}_n$ ($\Delta\sigma_{bt}/\bar{\sigma}_n < 6$), produced repetitive events which consistently ruptured through the bump. Fewer shims decreased the strength of the bump (smaller $\Delta\sigma_{bt}$). Higher $\bar{\sigma}_n$ caused higher local stress drop during rupture events, and a larger bump was required to stop those higher stress drop events. Thus, variable sequences were most likely to occur in experiments with many shims (large $\Delta\sigma_{bt}$) and at low $\bar{\sigma}_n$; ($\Delta\sigma_{bt}/\bar{\sigma}_n > 6$). In these variable sequences, all events appeared to initiate in the same location, and each event consisted of distinct, characteristic rupture phases. Larger rupture events always built upon the rupture phases of smaller rupture events, sometimes with a short (0.3–1 ms) pause between each phase of the rupture process, likely as a result of a finite re-nucleation time.

One particularly interesting case was when rupture bypassed the bump but the bump remained un-slipped. A rupture that stopped on one side of the bump could cause slip to re-nucleate on the opposite side of the bump without slipping the bump itself. This re-nucleation of rupture occurred not from the stress concentration at the rupture front but in response to elastic stress increase ahead of the arrested rupture front. Such stress increase is directly proportional to the stress drop within the ruptured region.

Our experiments and observations demonstrate how normal stress heterogeneity due to fault protuberances or stepovers can affect earthquake rupture patterns and cause rupture to terminate and reinitiate. On natural faults, these complexities to the rupture process likely occur at a variety of scales—since fault roughness and structure exists at various scales. At large scales, earthquake gates can cause complex long-term event histories with the behavior determined by stress conditions and other physical conditions (e.g., Rodriguez Padilla et al., 2022). Rupture complexities are manifest as complex source time functions (e.g., Yin et al., 2021) or as speedups and slowdowns in rupture velocity, that might be detectable with back-projection imaging (e.g., Mai et al., 2023; Meng et al., 2011). Our experiments show that this can also happen at a smaller scale: distinct rupture phases initiate and terminate as mediated by the bump. However, if a similar earthquake rupture process was observed using seismology and inferred through the analysis of radiated far-field seismic waves, the distinct rupture phases we observe may appear as a single rupture with variable velocity. Nevertheless, the rupture complexity associated with small scale fault heterogeneity is likely important for the generation of high frequency seismic radiation during the earthquake rupture process.

Appendix A: Composite Sample Details

The moving block (MB) is 740 mm by 200 mm by 38 mm in the x , y , z directions respectively (Figure 1b) and was made of 30 sub-blocks of poly (methyl-methacrylate) (PMMA) measuring ~ 25 mm by 200 mm by 38 mm (x , y , z). The sub-blocks were numbered MB#1–30, increasing in the positive x -direction. The stationary block is 778 mm by 149 mm by 38 mm (x , y , z) and was made of 33 sub-blocks of PMMA measuring ~ 25 mm by 149 mm by 38 mm (x , y , z). The sub-blocks were numbered SB#1–33, in the positive x -direction. Two holes were bored along the x -axis through each individual sub-block of PMMA, 25 mm from either end of the sub-blocks. Two 1/8" diameter threaded steel rods were run through these holes then tensioned by hand to hold the sub-blocks together. The length of the whole sample (740 mm MB, 778 mm SB) is slightly shorter than the sum of the nominal thicknesses of the individual blocks (750 mm MB, 825 mm SB) due to manufacturing inconsistency in the ~ 25 mm thickness in the x dimension. To prevent the sample from potentially buckling in the z -direction an anti-buckling system was created by placing a steel angle ($1.5 \times 1.5 \times 0.25$) on the top and bottom of both the MB and SB, shown as “steel support bar” in Figure 1b. Teflon was placed in the steel/PMMA interface to allow the PMMA composite sample to deform in the x - y plane without being restrained by friction between the steel and PMMA. The fault was prepared by sanding the PMMA surfaces with 80 grit sandpaper while using temporary acrylic “guides” attached to the sample to help enforce a planar interface. Even with these guides, the fault interface was not perfectly planar due to variations in alignment of the sub-blocks.

PMMA was chosen since it is easy to cut and machine and has small critical nucleation length. Nielsen et al. (2010) and Guérin-Marthe et al. (2019) recorded nucleation sizes of $h^* = 10$ –100 mm for polycarbonate at $\bar{\sigma}_n \approx 8$ MPa, and these estimates are generally consistent with our observations on solid PMMA samples (Cebry & McLaskey, 2021).

A1. Slip Between Sub-Blocks

When $\bar{\sigma}_n$ was increased with shims in place, the sub-blocks around the shims slipped in the y -direction. Due to friction between the sub-blocks (Figure 1c), they did not completely slip back to their original locations when the fault was unloaded (i.e., the bump was preserved by friction between the sub-blocks), and this caused a hysteresis effect with higher σ_b upon unloading $\bar{\sigma}_n$ than when increasing $\bar{\sigma}_n$. Even when the sample was removed from the apparatus, the blocks were visibly displaced near the bump. This effect was erased by loading the sample to a high normal stress with no shims.

A2. Comparison With Intact PMMA Sample

The behavior of the composite PMMA samples used in this study was compared to the behavior of standard samples with moving and stationary blocks made from single PMMA blocks with the same dimensions and fault preparation. Results for a set of standard stick-slip events at 10 MPa $\bar{\sigma}_n$ with zero shims are shown in Figure A1. Both samples produced a consistent set of complete-rupture stick-slip events. For both cases, the critical nucleation length, h^* , was less than the eddy current slip sensor spacing and ruptures appeared to be smooth and continuous, at least within the resolution of the slip sensor array. Compared to the intact samples, the composite samples had larger $\Delta\bar{\tau}_{\text{mech}}$, $\Delta\bar{x}$, and recurrence time but the fault strength $\bar{\tau}_p$ was lower. If we assume the composite sample without shims enabled a more homogeneous distribution of normal stress due to slip between the sub-blocks, then this behavior is consistent with the results of Xu et al. (2023). We measured the effective stiffness of the sample and apparatus, K , from complete, sample-spanning events with the equation, $K = \Delta\bar{\tau}_{\text{mech}}/\Delta\bar{x}$. The composite sample (with no shims) had a stiffness of 2.75 GPa/m which was somewhat less than the intact sample with a stiffness of 3.2 GPa/m.

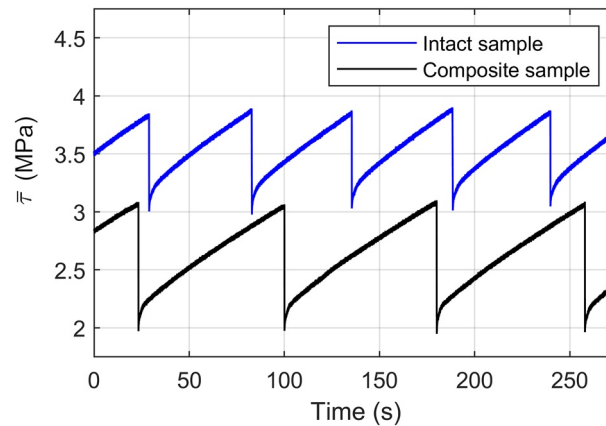


Figure A1. Comparison of shear stress versus time for the homogeneous sample and the composite sample with 10 MPa normal stress and an average loading rate of 0.2 $\mu\text{m/s}$.

Appendix B: 2D DIC Analysis

Samples were painted with a speckle pattern near the fault to use for 2D digital image correlation (DIC). A white background was painted using Krylon Fusion white spray paint. Then a random speckle pattern was created by flicking a paint brush dipped in red acrylic paint mixed with water. This created a random and distinct pattern necessary for DIC. The size of the speckles was varied by changing the ratio of acrylic paint to water and/or the amount of paint on the brush. The size of the speckles was chosen such that each speckle was approximately 2–20 pixels in the field of view chosen (Figure 3, Section 2.2).

We used DIC to measure both slip and stress along the fault. We developed in-house, MATLAB-based analysis software to best handle complexities caused by the many interfaces that make up the composite sample. In this analysis the user chooses the size, location, and number of discrete boxes from a reference image for correlation (Figures 3 and 7a). In both analyses the boxes were 30×30 pixels. In the large field of view for the normal stress benchmark test (Figure 3) the boxes corresponded to an area that was 2.7 mm by 2.7 mm and there were two

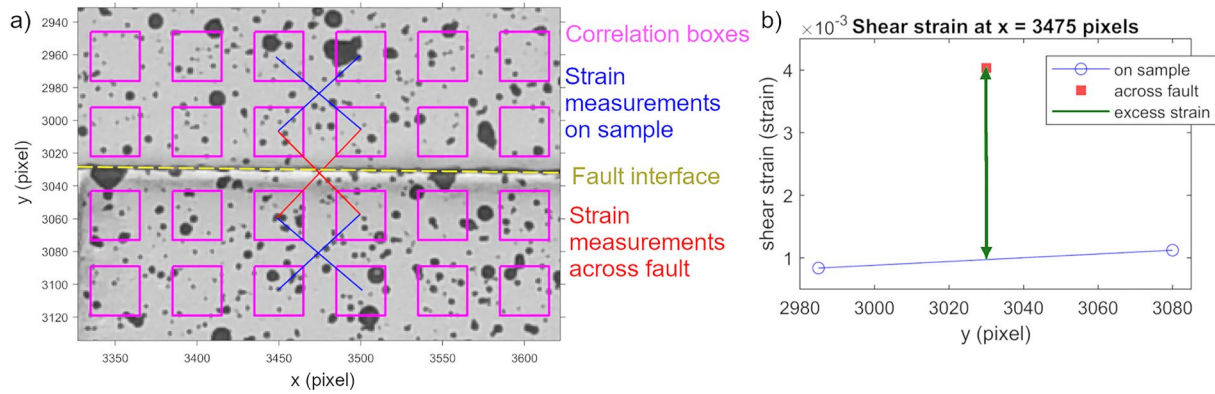


Figure B1. Example digital image correlation image with correlation boxes showing strain measured between four points then compared to on sample strain (blue) and across fault strain (red) measurements to determine the excess strain (green).

rows of 60 boxes set 12 mm apart on the moving block. In the small field of view used for the variable experiment (Figure 7a), the boxes covered an area that was 1.1 mm by 1.1 mm and there were four rows of 138 boxes set 1.8 mm apart. Boxes were chosen based on the speckle pattern, field of view, and desired spatial resolution. These boxes are correlated between the reference image and the rest of the images from the experiment using the MATLAB function `normxcorr2_general` (Figure 3). In the normal stress benchmark and the variable experiment, images were upsampled by a factor of 40 and 30, respectively, and the correlation was rerun for better resolution. This correlation provides a field of deformation measurements at the locations of each of the boxes. Linear-elasticity is assumed, and the deformation field is used to calculate stress and strain fields. This analysis uses a Young's modulus of 2.6 GPa and Poisson's ratio of 0.37 (Kammer et al., 2012). The 2D analysis assumed that there is no movement, and therefore no strain, in the z -direction.

The strain field was then used to calculate slip on the fault and other interfaces (Figure B1). This analysis assumed that shear strain is smooth and continuous across the fault interfaces. This analysis interpolates shear strain across the fault (blue line) based on measurements made from boxes that were all located on a single PMMA sub block (blue circles). The shear strain on the fault (red square) in excess of the interpolated shear strain (green line), is assumed to be slip and is converted from a strain to a displacement.

We quantify the resolution of our measurements with bounds on the minimum possible resolution and maximum noise based on the raw images, then note what the realistic noise is after analysis. For the large field of view, the minimum resolvable deformation was 0.025 pixels or 2.25 μm . For the small field of view, the minimum resolvable deformation was 0.033 pixels or 1.2 μm . To quantify the noise, we took two images of the sample in a similar set up back-to-back without making any changes to the sample. The maximum deformation measured between two images was 0.2 pixels which corresponds to 18 μm in the large field of view and 7.4 μm in the small field of view. In reality, the noise was lower than the peak deformation since we averaged over two boxes to make strain and stress measurements, but higher than the minimum resolvable because there is some noise. The assumed resolution is 0.1 pixels or 9 μm in the large field of view and 3.7 μm in the small field of view.

We convert the resolution into strain using the distance between correlation points. In the large field of view the box spacing was 12 mm which provided an ϵ_{xx} and ϵ_{yy} resolution of 7.7×10^{-4} (minimum resolvable: 1.9×10^{-4} , maximum peak noise: 1.5×10^{-3}) and ϵ_{xy} resolution of 5.4×10^{-4} (minimum: 1.4×10^{-4} , maximum: 1.1×10^{-3}). In the small field of view the box spacing was 1.8 mm which provided an ϵ_{xx} and ϵ_{yy} resolution of 2.0×10^{-3} (minimum: 6.7×10^{-4} , maximum: 4.0×10^{-3}) and ϵ_{xy} resolution of 1.4×10^{-3} (minimum: 4.7×10^{-4} , maximum: 2.8×10^{-3}). We use strain across the fault to measure slip with a minimum resolvable slip is 0.6 μm and noise level of 3.7 μm , however there is likely additional error from the assumption of continuous strain across the fault (Figure B1b). Overall, we confidently measure normal stress to within 5.6 MPa with a minimum resolution of 1.4 MPa in the large field of view used for Figure 3. In the small field of view used for Figure 7 we confidently measure slip to within 3.7 μm and shear stress to within 1.4 MPa with a minimum resolution of 0.47 MPa.

As a check of accuracy, we found $\overline{\sigma}_n$ measured from the hydraulic cylinders comparable to the average σ_n measured from DIC in Figure 3. For $\overline{\sigma}_n = 2$ and 8 MPa, the average σ_n obtained from DIC was $= 1.7$ and 12.6 MPa. Slip measurements in Figure 7 also were comparable to displacement sensor measurements off the bump (e.g., Figure 6, $x = 400$ mm).

Appendix C: Water Bucket Analogy

We can illustrate several of the concepts in this study by considering a line of buckets being filled with water (Figure C1). In this illustration, the volume of the buckets (the bucket capacity, depicted by the height of the bucket in the 2D drawing) represents the bump strength, τ_p , which is assumed to be proportional to normal stress $\tau_p = \mu_s \cdot \sigma_n$, where μ_s is the static coefficient of friction. A bump is a bucket that is larger than its neighboring buckets. The water represents shear stress. Slip initiation on a fault patch is represented as when a bucket fills with water and reaches capacity. Once full, the bucket partially tips over, representative of local fault slip, and splashes water into neighboring buckets, representative of elastic stress redistribution during rupture. The remaining water left in the tipped bucket represents the residual shear stress. Larger buckets, such as the one that represents the bump, spill more water when they tip than smaller buckets. The ability of each fault patch to accommodate shear stress without slipping at any given time is represented by empty volume of the buckets (total volume minus the volume of water). Following previous work (Boatwright & Quin, 1986), we term this the “strength excess” when

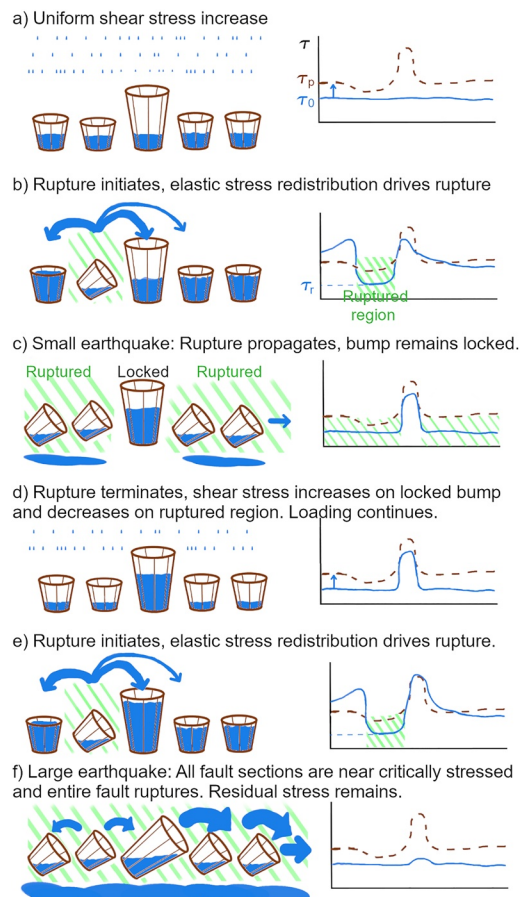


Figure C1. Cartoon conceptualization of relevant mechanisms. In this cartoon the size of the buckets represents the strength of the fault on different fault sections. The water represents shear stress. When the bucket fills with water, it tips over and spills water into the neighboring buckets, representative of elastic stress redistribution when the fault slips. If the neighboring bucket fills with water, it also tips and continues to spill water. If the neighboring bucket does not overflow, it remains locked. The large bucket represents the bump. It can accumulate more shear stress, but when the bump slips more shear stress is released.

referring to the experiments. Strength excess decreases when water is splashed into a bucket and increases when the bucket tips.

This analogy is helpful to understand why $\Delta\sigma_{bt}/\bar{\sigma}_n$ effects whether a bump stops rupture or not. In this analogy $\bar{\sigma}_n$ relates to the total volume of all the buckets and $\Delta\sigma_{bt}$ relates to how much larger the biggest bucket is compared to its neighbors. When the largest bucket is very large relative to the neighboring buckets, the small neighboring buckets must tip multiple times to fill the largest bucket. When the largest bucket is a similar size or just slightly larger than the rest of the buckets, it will be filled every time the neighboring small bucket tips.

In addition to explaining why a bump acts as a barrier, we can also illustrate how the bump acts as an asperity. In experiments with a prominent bump (large bump bucket) when the bump did finally slip, it released a large amount of the built-up strain energy in a complete-rupture event that was larger than those produced without a bump. Because the bump was near critically stressed, the small elastic stress change from rupture elsewhere on the fault was sufficient to initiate slip on the bump and unlock the strain energy stored in the bump. This is illustrated schematically in Figure C1e–C1f, where the large bucket tips and splashes much more water than any of the smaller buckets.

Data Availability Statement

Data is available at Cebry et al. (2023) and through Cornell eCommons at <https://doi.org/10.7298/0bdb-t883>.

References

- Aki, K. (1984). Asperities, barriers, characteristic earthquakes and strong motion prediction. *Journal of Geophysical Research*, 89(B7), 5867–5872. <https://doi.org/10.1029/JB089iB07p05867>
- Badt, N., Hatzor, Y. H., Toussaint, R., & Sagy, A. (2016). Geometrical evolution of interlocked rough slip surfaces: The role of normal stress. *Earth and Planetary Science Letters*, 433, 153–161. <https://doi.org/10.1016/j.epsl.2016.03.026>
- Bao, H., Xu, L., Meng, L., Ampuero, J.-P., Gao, L., & Zhang, H. (2022). Global frequency of oceanic and continental supershear earthquakes. *Nature Geoscience*, 15(11), 942–949. <https://doi.org/10.1038/s41561-022-01055-5>
- Bayart, E., Svetlizky, I., & Fineberg, J. (2018). Rupture dynamics of heterogeneous frictional interfaces. *Journal of Geophysical Research: Solid Earth*, 123(5), 3828–3848. <https://doi.org/10.1002/2018JB015509>
- Ben-David, O., Rubinstein, S., & Fineberg, J. (2010). Slip-stick and the evolution of frictional strength. *Nature*, 463(7277), 76–79. <https://doi.org/10.1038/nature08>
- Boatwright, J., & Quin, H. (1986). The seismic radiation from a 3-D dynamic model of a complex rupture process. Part I: Confined ruptures. In S. Das, J. Boatwright, & C. H. Scholz (Eds.), *Earthquake source mechanics*. <https://doi.org/10.1029/GM037p0097>
- Brodsky, E. E., McLaskey, G. C., & Ke, C.-Y. (2020). Groove generation and coalescence on a large-scale laboratory fault. *AGU Advances*, 1(4), e2020AV000184. <https://doi.org/10.1029/2020AV000184>
- Buijze, L., Guo, Y., Niemeijer, A. R., Ma, S., & Spiers, C. J. (2020). Nucleation of stick-slip instability within a large-scale experimental fault: Effects of stress heterogeneities due to loading and gouge layer compaction. *Journal of Geophysical Research: Solid Earth*, 125(8), e2019JB018429. <https://doi.org/10.1029/2019JB018429>
- Buijze, L., Guo, Y., Niemeijer, A. R., Ma, S., & Spiers, C. J. (2021). Effects of heterogeneous gouge segments on the slip behavior of experimental faults at dm scale. *Earth and Planetary Science Letters*, 554, 116652. <https://doi.org/10.1016/j.epsl.2020.116652>
- Candela, T., & Brodsky, E. E. (2016). The minimum scale of grooving on faults. *Geology*, 44(8), 603–606. <https://doi.org/10.1130/G37934.1>
- Caniven, Y., Dominguez, S., Soliva, R., Peyret, M., Cattin, R., & Maerten, F. (2017). Relationships between along-fault heterogeneous normal stress and fault slip patterns during the seismic cycle: Insights from a strike-slip fault laboratory model. *Earth and Planetary Science Letters*, 480, 147–157. <https://doi.org/10.1016/j.epsl.2017.10.009>
- Cattania, C., & Segall, P. (2021). Precursory slow slip and foreshocks on rough faults. *Journal of Geophysical Research: Solid Earth*, 126(4), e2020JB020430. <https://doi.org/10.1029/2020JB020430>
- Cebry, S. B. L., Ke, C.-Y., & McLaskey, G. C. (2022). The role of background stress state in fluid-induced aseismic slip and dynamic rupture on a 3-m laboratory fault. *Journal of Geophysical Research: Solid Earth*, 127(8), e2022JB024371. <https://doi.org/10.1029/2022JB024371>
- Cebry, S. B. L., Ke, C.-Y., Shreedharan, S., Marone, C., Kammer, D., & McLaskey, G. C. (2022). Creep fronts and complexity in laboratory earthquake sequences illuminate delayed earthquake triggering. *Nature Communications*, 13(6839), 6839. <https://doi.org/10.1038/s41467-022-34397-0>
- Cebry, S. B. L., & McLaskey, G. C. (2021). Seismic swarms produced by rapid fluid injection into a low permeability laboratory fault. *Earth and Planetary Science Letters*, 557, 116726. <https://doi.org/10.1016/j.epsl.2020.116726>
- Cebry, S. B. L., Sorhaindo, K., & McLaskey, G. C. (2023). Earthquake rupture interactions with a high normal stress bump [Dataset]. Cornell eCommons. <https://ecommons.cornell.edu/handle/1813/113268>
- Das, S., & Aki, K. (1977). Fault plane with barriers: A versatile earthquake model. *Journal of Geophysical Research*, 82(36), 5658–5670. <https://doi.org/10.1029/JB082i036p05658>
- Di Toro, G., Han, R., Hirose, T., De Paola, N., Nielsen, S., Mizoguchi, K., et al. (2011). Fault lubrication during earthquakes. *Nature*, 471(7339), 494–498. <https://doi.org/10.1038/nature09838>
- Duan, B., Liu, Z., & Elliott, A. J. (2019). Multicycle dynamics of the Aksay bend along the Altyn Tagh fault in northwest China: 2. The realistically complex fault geometry. *Tectonics*, 38(3), 1120–1137. <https://doi.org/10.1029/2018TC005196>
- Dunham, E. M., Belanger, D., Cong, L., & Kozdon, J. E. (2011). Earthquake ruptures with strongly rate-weakening friction and off-fault plasticity, Part 2: Nonplanar faults. *Bulletin of the Seismological Society of America*, 101(5), 2308–2322. <https://doi.org/10.1785/0120100076>

- Dunham, E. M., Favreau, P., & Carlson, J. M. (2003). A supershear transition mechanism for cracks. *Science*, 299(5612), 1557–1559. <https://doi.org/10.1126/science.1080650>
- Goebel, T. H. W., Becker, T. W., Schorlemmer, D., Stanchits, S., Sammis, C., Rybacki, E., & Dresen, G. (2012). Identifying fault heterogeneity through mapping spatial anomalies in acoustic emission statistics. *Journal of Geophysical Research*, 117(B3), B03310. <https://doi.org/10.1029/2011JB008763>
- Gounon, A., Latour, S., Letort, J., & El Arem, S. (2022). Rupture nucleation on a periodically heterogeneous interface. *Geophysical Research Letters*, 49(20), e2021GL096816. <https://doi.org/10.1029/2021gl096816>
- Guérin-Marthe, S., Nielsen, S., Bird, R., Giani, S., & Di Toro, G. (2019). Earthquake nucleation size: Evidence of loading rate dependence in laboratory faults. *Journal of Geophysical Research: Solid Earth*, 124(1), 689–708. <https://doi.org/10.1029/2018JB016803>
- Gvrtzman, S., & Fineberg, J. (2021). Nucleation fronts ignite the interface rupture that initiates frictional motion. *Nature Physics*, 17(9), 1037–1042. <https://doi.org/10.1038/s41567-021-01299-9>
- Herman, M. W., Furlong, K. P., & Govers, R. (2018). The accumulation of slip deficit in subduction zones in the absence of mechanical coupling: Implications for the behavior of megathrust earthquakes. *Journal of Geophysical Research: Solid Earth*, 123(9), 8260–8278. <https://doi.org/10.1029/2018JB016336>
- Kammer, D. S., Radiguet, M., Ampuero, J., & Molinari, J. (2015). Linear elastic fracture mechanics predicts the propagation distance of frictional slip. *Tribology Letters*, 57(3), 23. <https://doi.org/10.1007/s11249-014-0451-8>
- Kammer, D. S., Yastrebov, V. A., Spijker, P., & Molinari, J. F. (2012). On the propagation of slip fronts at frictional interfaces. *Tribology Letters*, 48(1), 27–32. <https://doi.org/10.1007/s11249-012-9920-0>
- Ke, C.-Y., McLaskey, G. C., & Kammer, D. S. (2018). Rupture termination in laboratory-generated earthquakes. *Geophysical Research Letters*, 45(23), 12784–12792. <https://doi.org/10.1029/2018GL080492>
- Ke, C.-Y., McLaskey, G. C., & Kammer, D. S. (2021). The earthquake arrest zone. *Geophysical Journal International*, 224(1), 581–589. <https://doi.org/10.1093/gji/ggaa386>
- Ke, C.-Y., McLaskey, G. C., & Kammer, D. S. (2022). Earthquake breakdown energy scaling despite constant fracture energy. *Nature Communications*, 13(1), 1005. <https://doi.org/10.1038/s41467-022-28647-4>
- Lay, T., & Kanamori, H. (1981). Earthquake prediction. *Maurice Ewing Series*, 579–592. <https://doi.org/10.1029/me004p0579>
- Lay, T., Kanamori, H., Ammon, C. J., Koper, K. D., Hutko, A. R., Ye, L., et al. (2012). Depth-varying rupture properties of subduction zone megathrust faults. *Journal of Geophysical Research*, 117(B4), B04311. <https://doi.org/10.1029/2011JB009133>
- Lay, T., Kanamori, H., & Ruff, L. (1982). The asperity model and the nature of large subduction zone earthquakes. *Earthquake Prediction Research*, 1, 3–71.
- Mai, P. M., Aspiotis, T., Aquib, T. A., Cano, E. V., Castro-Cruz, D., Espindola-Carmona, A., et al. (2023). The destructive earthquake doublet of 6 February 2023 in South-Central Türkiye and Northwestern Syria: Initial observations and analyses. *The Seismic Record*, 3(2), 105–115. <https://doi.org/10.1785/0320230007>
- McClay, K., & Bonora, M. (2001). Analog models of restraining stepovers in strike-slip fault systems. *AAPG Bulletin*, 85(2), 233–260. <https://doi.org/10.1306/8626C7AD-173B-11D7-8645000102C1865D>
- McLaskey, G. C. (2019). Earthquake initiation from laboratory observations and implications for foreshocks. *Journal of Geophysical Research: Solid Earth*, 124(12), 12882–12904. <https://doi.org/10.1029/2019JB018363>
- McLaskey, G. C., & Lockner, D. A. (2018). Shear failure of a granite pin traversing a sawcut fault. *International Journal of Rock Mechanics and Mining Sciences*, 110, 97–110. <https://doi.org/10.1016/j.ijrmm.2018.07.001>
- McLaskey, G. C., & Yamashita, F. (2017). Slow and fast ruptures on a laboratory fault controlled by loading characteristics. *Journal of Geophysical Research: Solid Earth*, 122(5), 3719–3738. <https://doi.org/10.1002/2016JB013681>
- Meng, L., Inbal, A., & Ampuero, J. (2011). A window into the complexity of the dynamic rupture of the 2011 mw 9 Tohoku-Oki earthquake. *Geophysical Research Letters*, 38(7), L00G07. <https://doi.org/10.1029/2011GL048118>
- Morad, D., Sagy, A., Tal, Y., & Hatzor, Y. H. (2022). Fault roughness controls sliding instability. *Earth and Planetary Science Letters*, 579, 117365. <https://doi.org/10.1016/j.epsl.2022.117365>
- Nielsen, S., Taddeucci, J., & Vinciguerra, S. (2010). Experimental observation of stick-slip instability fronts. *Geophysical Journal International*, 180(2), 697–702. <https://doi.org/10.1111/j.1365-246X.2009.04444.x>
- Ohnaka, M., & Shen, L. F. (1999). Scaling of the shear rupture process from nucleation to dynamic propagation: Implications of geometric irregularity of the rupturing surfaces. *Journal of Geophysical Research: Solid Earth*, 104(B1), 817–844. <https://doi.org/10.1029/1998JB900007>
- Oral, E., Ampuero, J. P., Ruiz, J., & Asimaki, D. (2022). A method to generate initial fault stresses for physics-based ground-motion prediction consistent with regional seismicity. *Bulletin of the Seismological Society of America*, 112(6), 2812–2827. <https://doi.org/10.1785/0120220064>
- Oskin, M., Elliott, A. J., Duan, B., Liu-Zeng, J., Liu, Z., Shao, Y., et al. (2015). Earthquake gates: Linking rupture length to geologically constrained dynamics of fault complexity, with examples from the Altyn Tagh and San Andreas faults. In *Abstract presented at 2015 GSA Annual Meeting*.
- Power, W. L., Tullis, T. E., Brown, S. R., Boitnott, G. N., & Scholz, C. H. (1987). Roughness of natural fault surfaces. *Geophysical Research Letters*, 14(1), 29–32. <https://doi.org/10.1029/GL014i001p00029>
- Rodríguez Padilla, A. M., Oskin, M. E., Rockwell, T. K., Delusina, I., & Singleton, D. M. (2022). Joint earthquake ruptures of the San Andreas and San Jacinto faults, California, USA. *Geology*, 50(4), 387–391. <https://doi.org/10.1130/G49415.1>
- Rubino, V., Lapusta, N., & Rosakis, A. J. (2022). Intermittent lab earthquakes in dynamically weakening fault gouge. *Nature*, 606(7916), 922–929. <https://doi.org/10.1038/s41586-022-04749-3>
- Schaal, N., & Lapusta, N. (2019). Microseismicity on patches of higher compression during larger-scale earthquake nucleation in a rate-and-state fault model. *Journal of Geophysical Research: Solid Earth*, 124(2), 1962–1990. <https://doi.org/10.1029/2018JB016395>
- Shi, Z., & Day, S. M. (2013). Rupture dynamics and ground motion from 3-D rough-fault simulations. *Journal of Geophysical Research: Solid Earth*, 118(3), 1122–1141. <https://doi.org/10.1002/jgrb.50094>
- Steinhardt, W., Dillavou, S., Agajanian, M., Rubinstein, S. M., & Brodsky, E. E. (2023). Seismological stress drops for confined ruptures are invariant to normal stress. *Geophysical Research Letters*, 50(9), e2022GL101366. <https://doi.org/10.1029/2022GL101366>
- Sudhir, K. (2022). Slip patterns on heterogeneous frictional interfaces [Doctoral Dissertation]. California Institute of Technology. <https://doi.org/10.7907/xkbp-ks08>
- Wu, B. S., & McLaskey, G. C. (2019). Contained laboratory earthquakes ranging from slow to fast. *Journal of Geophysical Research: Solid Earth*, 124(10), 10270–10291. <https://doi.org/10.1029/2019JB017865>
- Xu, S., Fukuyama, E., Yamashita, F., Kawakata, H., Mizoguchi, K., & Takizawa, S. (2023). Fault strength and rupture process controlled by fault surface topography. *Nature Geoscience*, 16(1), 94–100. <https://doi.org/10.1038/s41561-022-01093-z>

- Yamashita, F., Fukuyama, E., Xu, S., Kawakata, H., Mizoguchi, K., & Takizawa, S. (2021). Two end-member earthquake preparations illuminated by foreshock activity on a meter-scale laboratory fault. *Nature Communications*, *12*(1), 4302. <https://doi.org/10.1038/s41467-021-24625-4>
- Yin, J., Li, Z., & Denolle, M. A. (2021). Source time function clustering reveals patterns in earthquake dynamics. *Seismological Research Letters*, *92*(4), 2343–2353. <https://doi.org/10.1785/0220200403>
- Zehnder, A. (2012). In F. Pfeiffer & P. Wriggers (Eds.), *Lecture notes in applied and computational mechanics: Fracture mechanics* (p. 62). Springer.
- Zielke, O., Galis, M., & Mai, P. M. (2017). Fault roughness and strength heterogeneity control earthquake size and stress drop. *Geophysical Research Letters*, *44*(2), 777–783. <https://doi.org/10.1002/2016GL071700>